

# Carbon Isotopes Near Drip Lines in the Relativistic Mean-Field Theory

M.M. Sharma, S. Mythili and A.R. Farhan

*Physics Department, Kuwait University, Kuwait 13060*

(November 12, 2018)

## Abstract

We have investigated the ground-state properties of carbon isotopes in the framework of the relativistic mean-field (RMF) theory. RMF calculations have been performed with the non-linear scalar self-coupling of the  $\sigma$  meson using an axially symmetric deformed configuration. We have also introduced the vector self-coupling of the  $\omega$  meson for the deformed mean-field calculations. The results show that the RMF predictions on radii and deformations are in good agreement with the available experimental data. It is shown that several carbon isotopes possess a highly deformed shape akin to a superdeformation. The single-particle structure of nuclei away from the stability line has been discussed with a view to understand the properties near the neutron drip line. Predictions of properties of carbon isotopes away from the stability line are made.

## I. INTRODUCTION

Radioactive beams are being used increasingly to produce nuclei at the limits of the stability [1–5]. Nuclei near the neutron and proton drip lines are becoming accessible to experiments. Abnormally large reaction cross-sections for unstable nuclei near drip lines have been interpreted as existence of a large tail of neutron density in the exterior of nuclei. Consequently, the so called halo of particles has been hypothesized for nuclei near drip lines. The case of  $^{11}\text{Li}$  has attracted a widespread attention [6]. On one hand, properties of nuclei with halos and neutron skins are being synthesized and studied experimentally, these properties are providing a test bench to probe various theories and models, on the other hand. Description of very light nuclei in terms of a core and a set of valence particles hovering around the core are proving to be generally successful [7]. For nuclei with a larger number of particles, theories with an average field are being used increasingly. Thus, study of nuclei with a large range of isospin puts various theories and interactions to test their validity. At the same time, it should become possible to discern the isospin dependence of the nuclear force by studying nuclei at the extreme limits.

Relativistic Mean-Field (RMF) theory is one of the more successful ones in recent times for describing nuclei with a large range of isospin [8–12]. Earlier, the importance of the  $\rho$ -meson coupling and hence a proper asymmetry energy was emphasized by Sharma et al. [13]. Consequently, the RMF force NL-SH proved to be very successful in describing various facets of nuclear structure. Owing to a proper spin-orbit interaction in the RMF theory, it became possible to describe the anomalous isotope shifts of Pb nuclei [14]. It was shown [15–17] that ground-state properties of nuclei such as binding energies, charge and matter radii and deformation properties of nuclei over a large part of the periodic table are very well described within the RMF theory using the non-linear scalar self-coupling of  $\sigma$ -meson. The Dirac-Lorentz structure of the nuclear force and the nuclear saturation based upon the attractive component due to  $\sigma$ -meson and a repulsive component from  $\omega$ -meson make the RMF theory an attractive tool to study nuclear properties. An inherent spin-orbit

interaction arising from the Dirac-Lorentz structure of nucleons gives rise to appropriate shell effects. Such shell effects are duly responsible to explain the behaviour of isotope shifts in Pb and other nuclear chains [14,15]. Based upon the isospin dependence of the spin-orbit interaction in the RMF theory, the Modified Skyrme Ansatz (MSkA) [18] was proposed. Herein, the spin-orbit potential was proposed to contain only one-body contribution. The MSkA [18] was shown to exhibit shell effects which are in accord with the experimental data. Consequently, isotope shifts in Pb nuclei could be well reproduced with in the MSkA.

With the RMF theory having been developed to possess several advantages over the non-relativistic theories, we study here the ground-state properties of the chain of carbon isotopes. The carbon isotopes away from the stability line have been the focus of experimental study whereby interaction cross-sections for heavier carbon isotopes have been measured [19]. The matter and hence neutron radii of very neutron-rich isotopes have thus been deduced. The nuclear structure of nuclei away from the stability line and especially those in the vicinity of drip lines is not yet fully understood. A few attempts have been made to explore theoretically the ground-state properties of the carbon isotopes [20]. In the present work, we use the RMF theory to investigate systematically the nuclear structure of even-even carbon isotopes from proton drip line to the neutron drip line. We employ the non-linear scalar potential of the  $\sigma$ -meson as well as the model with the non-linear self-coupling of both the  $\sigma$  and  $\omega$  mesons. We will discuss the nuclear structure of carbon nuclei away from the stability line. A comparison will also be made with some results obtained using the relativistic Hartree-Bogoliubov approach. It will be interesting to see to what extent the mean-field approach will be able to describe the properties of known light nuclei such as carbon isotopes. In Section II, we present the formalism of the RMF theory and associated models of the  $\sigma$  and  $\omega$  meson potentials. The ensuing section provides details of the RMF calculations. In section IV we present the results and in the last section we will summarize our conclusions.

## II. RELATIVISTIC MEAN-FIELD THEORY

The starting point of the RMF theory is a Lagrangian density [8] where nucleons are described as Dirac spinors which interact via the exchange of several mesons. The Lagrangian density can be written in the following form:

$$\begin{aligned} \mathcal{L} = & \bar{\psi}(i\partial - M)\psi + \frac{1}{2}\partial_\mu\sigma\partial^\mu\sigma - U(\sigma) \\ & - \frac{1}{4}\Omega_{\mu\nu}\Omega^{\mu\nu} + \frac{1}{2}m_\omega^2\omega_\mu\omega^\mu + \frac{1}{4}g_4(\omega_\mu\omega^\mu)^2 - \frac{1}{4}\mathbf{R}_{\mu\nu}\mathbf{R}^{\mu\nu} + \frac{1}{2}m_\rho^2\boldsymbol{\rho}_\mu\boldsymbol{\rho}^\mu - \frac{1}{4}F_{\mu\nu}F^{\mu\nu} \\ & - g_\sigma\bar{\psi}\sigma\psi - g_\omega\bar{\psi}\omega\psi - g_\rho\bar{\psi}\boldsymbol{\rho}\boldsymbol{\tau}\psi - e\bar{\psi}\mathbf{A}\psi. \end{aligned} \quad (1)$$

The meson fields included are the isoscalar  $\sigma$  meson, the isoscalar-vector  $\omega$  meson and the isovector-vector  $\rho$  meson. The latter provides the necessary isospin asymmetry. The bold-faced letters indicate the isovector quantities. The model contains also a non-linear scalar self-interaction of the  $\sigma$  meson :

$$U(\sigma) = \frac{1}{2}m_\sigma^2\sigma^2 + \frac{1}{3}g_2\sigma^3 + \frac{1}{4}g_3\sigma^4 \quad (2)$$

The scalar potential (2) introduced by Boguta and Bodmer [21] has been found to be useful for an appropriate description of surface properties, although several variations of the non-linear  $\sigma$  and  $\omega$  fields have recently been proposed [22]. We have also included the vector self-coupling of the  $\omega$ -meson introduced by Bodmer [23]. The corresponding term in the Langrangian is represented by the coupling constant  $g_4$ . Here  $M$ ,  $m_\sigma$ ,  $m_\omega$  and  $m_\rho$  denote the nucleon-, the  $\sigma$ -, the  $\omega$ - and the  $\rho$ -meson masses, respectively, while  $g_\sigma$ ,  $g_\omega$ ,  $g_\rho$  and  $e^2/4\pi = 1/137$  are the corresponding coupling constants for the mesons and the photon.

The field tensors of the vector mesons and of the electromagnetic field take the following form:

$$\begin{aligned} \Omega^{\mu\nu} &= \partial^\mu\omega^\nu - \partial^\nu\omega^\mu \\ \mathbf{R}^{\mu\nu} &= \partial^\mu\boldsymbol{\rho}^\nu - \partial^\nu\boldsymbol{\rho}^\mu - g_\rho(\boldsymbol{\rho} \times \boldsymbol{\rho}) \\ F^{\mu\nu} &= \partial^\mu\mathbf{A}^\nu - \partial^\nu\mathbf{A}^\mu \end{aligned} \quad (3)$$

The variational principle gives rise to the equations of motion. Our approach includes the time reversal and the charge conservation. The Dirac equation can be written as:

$$\{-i\alpha\nabla + V(\mathbf{r}) + \beta[M + S(\mathbf{r})]\} \psi_i = \epsilon_i \psi_i \quad (4)$$

where  $V(\mathbf{r})$  represents the *vector* potential:

$$V(\mathbf{r}) = g_\omega \omega_0(\mathbf{r}) + g_\rho \tau_3 \rho_0(\mathbf{r}) + e \frac{1 + \tau_3}{2} \mathbf{A}_0(\mathbf{r}) \quad (5)$$

and  $S(\mathbf{r})$  is the *scalar* potential:

$$S(\mathbf{r}) = g_\sigma \sigma(\mathbf{r}) \quad (6)$$

the latter gives rise to the effective mass as:

$$M^*(\mathbf{r}) = M + S(\mathbf{r}) \quad (7)$$

The Klein-Gordon equations for the meson fields are time-independent inhomogenous equations with the nucleon densities as sources.

$$\begin{aligned} \{-\Delta + m_\sigma^2\} \sigma(\mathbf{r}) &= -g_\sigma \rho_s(\mathbf{r}) - g_2 \sigma^2(\mathbf{r}) - g_3 \sigma^3(\mathbf{r}) \\ \{-\Delta + m_\omega^2\} \omega_0(\mathbf{r}) &= g_\omega \rho_v(\mathbf{r}) - g_4 \omega_0^3(\mathbf{r}) \\ \{-\Delta + m_\rho^2\} \rho_0(\mathbf{r}) &= g_\rho \rho_3(\mathbf{r}) \\ -\Delta A_0(\mathbf{r}) &= e \rho_c(\mathbf{r}) \end{aligned} \quad (8)$$

where  $\omega_0(r)$  and  $\rho_0(r)$  are the time-like components of the  $\omega$  and  $\rho$  meson fields. The corresponding source terms are

$$\begin{aligned}
\rho_s &= \sum_{i=1}^A \bar{\psi}_i \psi_i \\
\rho_v &= \sum_{i=1}^A \psi_i^+ \psi_i \\
\rho_3 &= \sum_{p=1}^Z \psi_p^+ \psi_p - \sum_{n=1}^N \psi_n^+ \psi_n \\
\rho_c &= \sum_{p=1}^Z \psi_p^+ \psi_p
\end{aligned} \tag{9}$$

where the sums are taken over the valence nucleons only. In the the present approach we neglect the contributions of negative-energy states (*no-sea* approximation), i.e. the vacuum is not polarized. The Dirac equation is solved using the oscillator expansion method [24].

The centre-of-mass correction to the total energy is included by taking the centre-of-mass energy based upon the harmonic oscillator prescription as given by

$$E_{cm} = \frac{3}{4} \hbar \omega \tag{10}$$

### III. DETAILS OF CALCULATIONS

The RMF calculations have been performed in a cylindrical basis where axial symmetry has been maintained. The fermionic and bosonic wavefunctions are expanded in a basis of harmonic oscillator. For the expansion, we have taken 12 shells for the fermionic as well as bosonic wavefunctions.

The pairing has been included using the BCS formalism. We have used constant pairing gaps which are obtained using the prescription of Möller and Nix [25] as given by

$$\begin{aligned}
\Delta_n &= \frac{4.8}{N^{1/3}} \\
\Delta_p &= \frac{4.8}{Z^{1/3}}
\end{aligned} \tag{11}$$

Only a few empirical data on the pairing gaps are available in this chain. The pairing gaps obtained for a few nuclei from the experimental binding energies are found to be

consistent with the above prescription. The centre-of-mass correction is included by using the zero-point energy of a harmonic oscillator as in Ref. [24]

We have used the RMF force NL-SH [13] for the Lagrangian with the non-linear scalar coupling. This force has been employed widely to describe properties of several chains of nuclei. It is known to provide excellent results for nuclei on both the sides of the stability line. This force has been found to be especially useful for nuclei far away from the stability line.

For the Lagrangian with the vector self-coupling, we have used the force TM1 [26]. We have also used a newly developed force NL-SV1 [27] which has been obtained by an exhaustive study of the ground-state properties of nuclei within the framework of the non-linear scalar and non-linear vector self-coupling. The details about NL-SV1 will be provided elsewhere. The parameters and coupling constants of the forces we have used are given in Table I.

## IV. RESULTS AND DISCUSSION

### A. Binding Energies

The binding energy of carbon isotopes in the deformed RMF calculations with the non-linear scalar force NL-SH and with the non-linear scalar-vector forces TM1 and NL-SV1 are shown in Table II. The values correspond to the lowest energy for the ground state. As carbon isotopes are perceived to be deformed, the RMF minimization was performed both for a prolate and an oblate shape. The corresponding deformation for the lowest minimum and a secondary minimum (if existent) will be discussed below. The binding energy for the secondary minimum are given in parentheses. Experimental values from the mass compilation of Audi and Wapstra [28] are also shown for comparison.

It is seen that the force NL-SH describes the binding energies of light carbon isotopes well. For the heavier isotopes, the force NL-SH gives a slight overbinding. In comparison,

The force TM1 gives an equally good description for the lighter nuclei. It is observed that NL-SH which is a force with a scalar self-coupling of  $\sigma$ -meson only and TM1 which includes also the self-coupling of  $\omega$ -meson produce binding energies which are very close to each other for light as well as medium-heavy carbon nuclei. Whilst NL-SH lends an additional binding of about 1-2 MeV to the heavier carbon isotopes as compared to the experimental values, TM1 provides a stronger overbinding to heavier carbon nuclei as compared to the NL-SH results as well as the experimental values.

The scalar-vector force NL-SV1, on the other hand, underestimates the binding of the very light carbon isotopes slightly. For the other carbon isotopes, the agreement of the NL-SV1 binding energies with the experimental values is qualitatively better than those of NL-SH and TM1. A comparison of predictions of various forces with the experimental data shows that the RMF theory provides a good description of the binding energies of carbon isotopes.

## B. The Quadrupole Deformation

The quadrupole deformation  $\beta_2$  and the quadrupole moment  $Q_2$  obtained from the relativistic Hartree minimization with various forces are shown in Fig 1. The  $\beta_2$  and  $Q_2$  values are given in Table III. The deformation parameters for NL-SH (Fig. 1.a) show that in the lowest-energy state the nucleus  $^{10}\text{C}$  is highly prolate ( $\beta_2 \sim 0.54$ ). This nucleus also exhibits a secondary minimum with an oblate shape ( $\beta_2 \sim -0.16$ ). The behaviour of  $\beta_2$  using the forces with the scalar-vector coupling is very different for this nucleus. Both the forces TM1 (Fig. 1.b) and NL-SV1 (Fig. 1.c) predict a well deformed oblate shape with  $\beta_2 \sim -0.29$  and  $\beta_2 \sim -0.21$ , respectively, for this nucleus. It can be seen from Table III that a highly deformed (akin to superdeformation) secondary minimum is also exhibited by this nucleus with TM1 ( $\beta_2 \sim 0.64$ ) and NL-SV1 ( $\beta_2 \sim 0.58$ ).

The stable nucleus  $^{12}\text{C}$  is described as oblate shaped by all the three forces. It is shown to be less deformed with NL-SH as compared with TM1 and NL-SV1. TM1, in particular, gives

this nucleus a strongly deformed oblate shape ( $\beta_2 \sim -0.39$ ). Whilst TM1 and NL-SV1 give a single well-defined oblate minimum for  $^{12}\text{C}$ , NL-SH also predicts a spherical secondary minimum only about 100 keV above the lowest minimum (see Table II). A comparison of the  $\beta_2$  values from RMF with the available experimental information will be in order. The quadrupole deformation for  $^{12}\text{C}$  has been estimated using various experimental probes. Analysis of inelastic  $\alpha$ -scattering experiment [29] led to a value of  $\beta_2 \sim -0.29$ . However, another experiment [30] with inelastic  $\alpha$ -scattering reported a value of  $\beta_2 = -0.40$ . In comparison, a value of  $\beta_2 \sim -0.41$  has been deduced [31] using inelastic scattering of triton beam. Similar oblate deformations have also been deduced from inelastic electron scattering [32]. All these experiments demonstrate unequivocally that  $^{12}\text{C}$  has an oblate shape in its ground state. The RMF theory with both the scalar self-coupling as well as with scalar-vector self-coupling models describes the deformation of  $^{12}\text{C}$  very well. The deformations predicted by the scalar-vector coupling models support several experimental deductions.

The nucleus  $^{14}\text{C}$  with the magic neutron number  $N=8$ , and its neighbour  $^{16}\text{C}$  are both shown to be spherical with all the three forces. However, for nuclei above  $N=10$ , the influence of the magic number  $N=8$  diminishes rapidly and consequently the nuclei  $^{18}\text{C}$ ,  $^{20}\text{C}$  and  $^{22}\text{C}$  take up a well-deformed oblate shape in RMF calculations with all the three forces. It is seen that there is an abrupt onset of deformation as 2 neutrons are added to the spherical nucleus  $^{16}\text{C}$ . The resulting deformation for  $^{18}\text{C}$  is predicted to be less than that for  $^{20}\text{C}$  for any given force. The nucleus  $^{20}\text{C}$  with  $N=14$  is well in the middle of the shell where the largest value of  $\beta_2$  is obtained (see Table III). A further addition of a pair of neutrons also brings about a well-deformed oblate shape for  $^{22}\text{C}$ . The magnitude of  $\beta_2$  for  $^{22}\text{C}$  is lower than that for  $^{20}\text{C}$ . As the magic number  $N=20$  approaches, nuclei assume a spherical shape.

A comparative look at the values of  $\beta_2$  and  $Q_2$  amongst the three forces shows that for nuclei  $A=18-22$ , the force NL-SH produces the lowest deformation, whereas TM1 is shown to provide the largest value. The force NL-SV1, on the other hand, gives a value of  $\beta_2$  which lies between that of NL-SH and TM1. Whilst TM1 and NL-SV1 predict shape coexistence only for  $^{10}\text{C}$ , NL-SH is shown to give a secondary minimum with another shape for several

nuclei.

A comment on the deformation properties of carbon isotopes in various mean-field theories will be appropriate to make here. The mean-field theories, in particular, those of the density-dependent Skyrme type have generally given a spherical shape to the nucleus  $^{12}\text{C}$ . This nucleus is widely perceived to be oblate shaped. The RMF theory predicts such a shape and especially the scalar-vector model gives a highly deformed oblate quadrupole deformation for  $^{12}\text{C}$ .

### C. Neutron-Proton Deformations

The difference in the quadrupole deformation of the neutron and proton densities are shown in Fig. 2. The figure shows that for  $^{10}\text{C}$ , the deformation for neutrons and protons is the same with NL-SH, although the  $\beta_2$  value is very large ( $\sim 0.54$ ) in the lowest energy state. The model with the scalar-vector self-coupling does show a difference in the deformation of neutrons and protons. As discussed above, forces TM1 and NL-SV1 with these models predict an oblate shape for  $^{12}\text{C}$ . Both these forces also show the difference  $\beta_n - \beta_p$  as positive. This implies that the proton field is more deformed than the neutron field. TM1 predicts this difference ( $\sim 0.05$ ) to be slightly higher than NL-SV1.

The  $\beta_n - \beta_p$  is close to zero for  $^{12}\text{C}$  with all the three forces although TM1 and NL-SV1 predict a stronger oblate shape than NL-SH. The nuclei  $^{14}\text{C}$  and  $^{16}\text{C}$  are spherical and hence there is a vanishing  $\beta_n - \beta_p$ . For the nuclei  $^{18}\text{C}$ ,  $^{20}\text{C}$  and  $^{22}\text{C}$ , a marked difference in the deformations of neutron and proton fluids is seen. All these nuclei are neutron rich and predicted to be oblate shaped with significantly large  $\beta_2$  values. A large negative value of  $\beta_n - \beta_p$  for these nuclei means that neutron deformation is considerably larger than the corresponding proton deformation. The neutron number for these nuclei is 12, 14 and 16, respectively. The neutron deformation  $\beta_n$  is accentuated by these numbers being in the middle of the neutron shell. The onset of the deformation at  $A=18$  corresponds closely to a significant occupation of the  $\Omega^\pi = [202]3/2^+$  orbital. At the same time, there is a substantial

lowering of this level as  $A=18$  ( $N=12$ ) approaches. Details of single-particle structure will be discussed in Section IV.E.

#### D. Nuclear Radii and Densities

The *rms* radii for neutron, charge and nuclear matter for the carbon nuclei are shown in Fig. 3. The values of radii are presented in Tables IV and V. The charge radius is obtained by folding the *rms* proton radius with the finite proton size. Experimental matter radii deduced from total reaction cross sections and neutron radii deduced therefrom [19] are also given in Table IV. The radii shown in the figures correspond to the shape for the lowest energy state.

The charge radius of carbon isotopes shows a roughly constant value for most of the nuclei with all the forces. Only for  $^{10}\text{C}$ , there is a significant increase in the charge radius as compared to  $^{12}\text{C}$ . This is due to the onset of proton drip line in going to the more neutron-deficient isotopes. For isotopes heavier than  $^{12}\text{C}$ , the charge radius shows only a marginal increase as pairs of neutrons are added. Such a behaviour is common to most isotopic chains.

The charge radii predicted by the various RMF forces are given in Table V. Charge radii of  $^{12}\text{C}$  and  $^{14}\text{C}$  from elastic electron scattering data [33] are also shown in the table. The experimental value of the charge radius is estimated at  $2.47 \pm 0.02$  fm for  $^{12}\text{C}$  and at  $2.56 \pm 0.05$  fm for  $^{14}\text{C}$ . In comparison the force NL-SH predicts the charge radius for  $^{12}\text{C}$  as 2.66 fm and both TM1 and NL-SV1 give it at about 2.7 fm. Thus, the RMF theory overestimates the charge radius of  $^{12}\text{C}$  slightly. An explicit centre-of-mass correction might improve the predicted value.

The *rms* neutron radius shows a steady increase from  $A=10$  to  $A=14$  for all the forces (see Fig. 3). However, for nuclei above  $A=14$  there is a sudden increase in value. The increase in the neutron radius is shown to be phenomenal for  $^{16}\text{C}$  as compared to  $^{14}\text{C}$  in all the models. Such an increase in the *rms* neutron radius by  $\sim 0.5$  fm is obviated by a major shell gap at  $N=8$ . The increase in the neutron radius for the isotopes heavier than  $^{16}\text{C}$  is

modest with a successive addition of a pair of neutrons. This increase in the neutron *rms* radius increases the neutron skin of the heavier carbon isotopes. It is seen that the neutron radius of  $^{24}\text{C}$  is only marginally larger than its lighter neighbour  $^{22}\text{C}$ . The magnitude of the increase in the *rms* neutron radius of  $^{24}\text{C}$  or of any of its neighbours is not so much as to characterize this as a neutron halo. It may be noted that  $^{24}\text{C}$  is predicted to be near the neutron drip line in all the forces. Thus, it is concluded that the neutron halo is not present in the carbon isotopes near the neutron drip line.

The matter radii as shown in Fig. 3 reflect much the behaviour of the neutron radii. It is noteworthy that the features presented by various *rms* radii for the carbon isotopes are similar for both the models with scalar self-coupling as well as with the scalar-vector self-coupling. There is also a similarity between the results of TM1 and NL-SV1.

A comparison of the predictions of RMF matter and neutron radii with the experimental values (Table IV) shows that the RMF values describe the data very well. Predictions of all the forces are within the error bars. Even for the heavier carbon isotopes such as  $^{16}\text{C}$  and  $^{18}\text{C}$  the RMF values show a very good agreement with the experimental data. Thus, the RMF theory is able to provide reliable predictions of the properties away from the stability line.

In Fig. 3a, we also show neutron radii taken from the spherical Relativistic Hartree-Bogoliubov (RHB) calculations [34] using the force NL3. Herein, the finite-range Gogny pairing was included. The RHB calculations take into account the effect of states near the continuum appropriately. As the force NL3 is known to give results very close to those of NL-SH, a comparison of the NL3 results with those of NL-SH is worthwhile. The comparison of the RHB neutron radii with the RMF+BCS results shows that the RHB values are very similar to the RMF+BCS ones. Especially, for spherical nuclei such as  $^{16}\text{C}$  and  $^{24}\text{C}$ , the agreement between our results and those of the RHB is remarkable. This suggests that the effect of the continuum on the carbon nuclei near neutron drip line may not be significant. It is, however, not clear why RHB underestimates the neutron radius of  $^{12}\text{C}$ .

The  $L=0$  component of the vector ( $\rho_v$ ) and scalar ( $\rho_s$ ) neutron density for the carbon

isotopes is shown in Fig. 4 for the forces NL-SH, TM1 and NL-SV1. Both the vector and scalar densities show a similar behaviour. The scalar densities are slightly smaller than the corresponding vector (baryonic) densities. The difference in the vector and scalar densities is representative of the relativistic effects in the nuclear structure.

The increase in the radial extension of the densities is seen clearly as the neutron number increases. The increase in the densities of heavier carbon isotopes above  $^{14}\text{C}$  is mostly in the exterior of nuclei, thus contributing to an increasingly large neutron skin as more neutrons are added. However, for the highly deformed carbon nuclei a considerable part of densities lies in the exterior of the quadrupole ( $L=2$ ) component. Figure 5 shows the  $L=2$  component of the neutron vector density  $\rho_v$  obtained with the RMF forces for the three oblate deformed nuclei  $^{18}\text{C}$ ,  $^{20}\text{C}$  and  $^{22}\text{C}$ . The negative density implies that the neutron matter is missing at the poles as compared to a spherical shape. The corresponding matter is accumulated along the equatorial plane.

As shown above the nuclei  $^{18}\text{C}$ ,  $^{20}\text{C}$  and  $^{22}\text{C}$  are predicted to be oblate shaped with all the three forces. As we have seen, there are slight differences in predictions of the magnitude of the quadrupole deformation between various forces. The  $L=2$  component of the density is sensitive to these differences in the deformation. The  $L=2$  densities show a negative peak which changes its position slightly about 2.5 fm from one nucleus to another.

The densities given in Fig. 5a for the force NL-SH show that the nucleus  $^{18}\text{C}$ , which has  $\beta_2 \sim -0.32$ , has the smallest  $L=2$  component as compared to  $^{20}\text{C}$  which has  $\beta_2 \sim -0.41$ . For  $^{22}\text{C}$  the  $L=2$  peak is smaller than that for  $^{20}\text{C}$  as  $\beta_2$  for  $^{22}\text{C}$  is  $\sim -0.31$  which is smaller than that for  $^{20}\text{C}$ . However, the peak for  $^{22}\text{C}$  is bigger than that for  $^{18}\text{C}$  due to a larger quadrupole moment for the latter.

A comparison of the  $L=2$  densities for the various forces shows that except for a slight variation in the depths of the peaks due to varying  $\beta_2$  values and quadrupole moments, the features of the  $L=2$  densities are very similar. This is primarily due to the reason that all the three forces considered here predict an overwhelmingly oblate shape for these nuclei and that the variation in the deformation in various models is similar from one nucleus to

another.

We show in Fig. 6 the  $L=0$  component of the proton vector density for  $^8\text{C}$ ,  $^{10}\text{C}$  and  $^{12}\text{C}$ . The lighter nuclei  $^{10}\text{C}$  and  $^8\text{C}$  are proton rich and it is interesting to see how the proton density changes as one approaches the proton drip line. Calculations with the force NL-SH (Fig. 6a) show that the proton density in the interior of the nucleus  $^{10}\text{C}$  decreases as compared to that in  $^{12}\text{C}$ . The decrease in the central density in interior of  $^8\text{C}$  over its heavier counterparts is seen to be substantial. This takes place at the expanse of the proton density at the surface. However, the spatial extension of the proton density is not so much as to characterize it as a proton halo. This is due to the Coulomb barrier which inhibits formation of a proton halo.

The behaviour of the proton density for the forces TM1 and NL-SV1 with the scalar-vector self-coupling is not very different from that of NL-SH. Due to slightly different predictions of deformation for  $^{12}\text{C}$  and  $^{10}\text{C}$  by these forces as compared to NL-SH (see Table III), densities of these two isotopes with scalar-vector forces is only slightly different than with NL-SH. The behaviour of the density of  $^8\text{C}$  is similar with all the three forces. It may be pointed out that the densities of  $^8\text{C}$  are presented here only for a qualitative comparison.

### E. Single-Particle Levels

In order to visualize the single-particle levels contributing to the evolution of the properties of carbon isotopes as a function of neutron number, we show the single-particle levels for NL-SH and NL-SV1 in Figs. 7 and 8, respectively. The upper panel shows the levels just below the continuum. In the lower panel, we show only a few levels which are not so deep lying. The levels are identified by the quantum number  $\Omega^\pi$  consistent with the Nilsson scheme [35]. The numbers in the parentheses indicate the quantum numbers  $[\text{Nn}_z\Lambda]$ . Occupancy in the few highest lying  $\Omega$  orbitals is shown in Fig. 9 for NL-SH and NL-SV1. Here we show a comparison only between NL-SH and NL-SV1 which represent the scalar self-coupling and scalar-vector self-coupling models, respectively. The single-particle properties of the force

TM1 are expected to be similar to that of NL-SV1.

The lower panel of Fig. 7 shows that for the nuclei  $^{10}\text{C}$  and  $^{12}\text{C}$  which are predicted to be deformed (see Table III), the level  $p_{3/2}$  splits into  $[101]3/2^-$  and  $[110]1/2^-$ . The nucleus  $^{10}\text{C}$  being predicted as highly prolate with NL-SH, the orbital  $[101]3/2^-$  lies higher than  $[110]1/2^-$ . As one moves to  $^{12}\text{C}$ , the two orbitals cross and the orbital  $[101]3/2^-$  is suppressed in energy as a consequence of the oblate shape of this nucleus as predicted by NL-SH. These two orbitals are degenerate for  $^{14}\text{C}$  and  $^{16}\text{C}$  both of which are spherical. The degeneracy in the two orbitals is lifted again for the heavier carbon isotopes  $^{18}\text{C}$ ,  $^{20}\text{C}$  and  $^{22}\text{C}$  which are all predicted to be oblate shaped. The splitting between the two  $\Omega$  partners amounts to about 10 MeV for these nuclei. Interestingly, the  $[110]1/2^-$  orbital is lifted up significantly as compared to its degenerate (unperturbed) position.

The behaviour of the orbital  $[101]1/2^-$  corresponding to the  $p_{3/2}$  level, is seen to be influenced considerably by the presence of deformation. For the deformed nuclei and particularly those with an oblate shape, the orbital  $[101]1/2^-$  is lowered significantly in energy as compared to the position in spherical case. For the prolate shaped nucleus  $^{10}\text{C}$  the opposite is true.

For the force NL-SV1, the behaviour of the three orbitals below  $-10$  MeV is very similar to that for NL-SH, as shown in the lower panel of Fig. 8. As both  $^{10}\text{C}$  and  $^{12}\text{C}$  are predicted to be oblate, the crossing of  $[101]3/2^-$  and  $[110]1/2^-$  is not observed. Moreover, the splitting between these two levels is proportionate to the  $\beta_2$  value  $-0.21$  and  $-0.33$  for  $^{10}\text{C}$  and  $^{12}\text{C}$ , respectively, as can be noticed readily from the figure.

For nuclei up to  $A=14$  ( $N=8$ ), orbitals corresponding to the levels  $1s1/2$ ,  $1p3/2$  and  $1p1/2$  are filled successively. For nuclei above  $^{14}\text{C}$ , the levels in the next shell start filling. The upper panel of Figs. 7 and 8 show the single-particle levels in this shell. These levels lie in the neighbourhood of the Fermi surface which is shown by the dotted line. The levels include  $\Omega$  orbitals for  $1d5/2$ ,  $2s1/2$  and  $1d3/2$ . As the predictions of NL-SH and NL-SV1 on the deformations for  $A > 16$  are similar, the single-particle structure in both Figs. 7 and 8 is similar.

The three  $\Omega$  components for the  $1d5/2$  level are shown by the dotted curve. These are degenerate for the spherical shape at  $A=16$ . It is seen that as the deformed shape evolves for  $A = 18, 20$  and  $22$  on adding neutrons to  $A = 16$ , the orbital  $[202]5/2^+$  corresponding to  $1d5/2$  with the largest  $\Omega$  value is suppressed. Part of this lowering is also expected from the increase in the depth of the potential well for nuclei richer in neutrons. The counterparts with lower  $\Omega$  values e.g.  $[211]3/2^+$  and  $[220]1/2^+$  are, on the other hand, lifted up in energy for the deformed isotopes  $^{18}\text{C}$ ,  $^{20}\text{C}$  and  $^{22}\text{C}$ . The three  $\Omega$  components converge for  $^{24}\text{C}$  which is close to being spherical. The  $[200]1/2^+$  component corresponding to  $2s1/2$  level is close to being degenerate with the  $1d5/2$  level for the nucleus  $^{16}\text{C}$ . The orbital  $[200]1/2^+$  follows a mild lowering in energy with an increase in  $A$ .

The  $\Omega$  orbitals  $[202]3/2^+$  and  $[211]1/2^+$  for  $1d3/2$  level also show a significant splitting for the deformed nuclei, the larger  $\Omega$  orbital being lowered in energy. The consequence of the splitting between various  $\Omega$  orbitals shown in the upper panel of Figs. 7 and 8 is that there is a gap of about 3-4 MeV in the energy levels, which persists for  $A=18-22$ .

Figures 7 and 8 show how the Fermi energy is changing with neutron number. For  $^{16}\text{C}$ , the Fermi energy decreases rapidly as compared to  $^{14}\text{C}$ . This is due to the onset of the next shell for neutrons. Above  $^{16}\text{C}$ , the Fermi energy decreases slowly and approaches the vanishingly small value for  $^{24}\text{C}$ . This indicates the onset of the neutron drip line. Such a behaviour is similar for NL-SH as well as NL-SV1.

We show in Fig. 9 the occupation probabilities for some of the orbitals close to the Fermi energy. The orbitals are arranged in order of increasing energy. Owing to the similarities in the predictions of the deformations, the behaviour of the occupation numbers is similar for NL-SH and NL-SV1 for the levels which are significant only for the very neutron-rich carbon isotopes. The level  $[202]5/2^+$  is filled up significantly already at  $A=18$ . The neighbouring levels  $[200]1/2^+$  and  $[202]3/2^+$  (see Figs. 7 and 8) also show a considerable occupancy at  $A=18$  and are being filled up increasingly up to  $A=22$ . The bunch of three levels  $[202]5/2^+$ ,  $[200]1/2^+$  and  $[202]3/2^+$  is responsible for maintaining a very large oblate deformation for carbon isotopes with  $A = 18, 20$  and  $22$ . The levels  $[211]1/2^+$  and  $[211]3/2^+$  play only a

lesser role for these nuclei. The latter is filled up only for  $A=24$  which is predicted to be spherical. The population of the orbital  $[202]3/2^+$   $^{24}\text{C}$  is quenched as this levels comes up again near the continuum in its unperturbed position for the spherical shape.

In Fig. 10 we show the shapes of a few highly deformed oblate and prolate configurations of carbon isotopes. The vertical axis in each figure is the axis of symmetry. The nucleus  $^{10}\text{C}$  has an oblate shape in the ground state as discussed above. This nucleus is also shown to give a secondary minimum with a highly prolate shape. Both NL-SV1 and TM1 forces give a similar predictions for the deformation. It is instructive to compare the single-particle structure of  $^{10}\text{C}$  for the oblate and the prolate shapes. The single-particle structure for the two shapes is shown in Fig. 11. As there are only 4 protons in  $^{10}\text{C}$ , two protons go inevitably to the  $1s1/2$  level. The other two protons go to the second shell. For the oblate shape, the  $\Omega^\pi = 3/2^-$  orbital is lower in energy and the splitting between the  $\Omega^\pi = 3/2^-$  and  $\Omega^\pi = 1/2^-$  is small. For the prolate shape, the lower  $\Omega^\pi = 1/2^-$  orbital is suppressed in energy and contains a sizeable fraction of the nucleon occupancy. The splitting between the two  $\Omega^\pi$  orbitals is obviously larger for the case of the prolate shape (due to a larger value of  $\beta_2$ ) than the oblate case. The gap between the  $1s1/2$  level and the next shell is about 17.5 MeV for the prolate shape. The large deformation  $\beta_2 = 0.59$  achieved using the force NL-SV1 and a larger value  $\beta_2 = 0.64$  obtained for TM1 correspond to the so-called superdeformation of nuclei whereby a 2:1 ratio of the axes are achieved within a harmonic oscillator scheme. This also leads to a creation of new shells in the deformation space [35]. The oscillator frequencies  $\omega_\perp : \omega_z$  for the prolate shape are in the ratio  $1.76 : 1$ , which lies in the vicinity of the ideal value  $2 : 1$  for the oscillator potential. Thus,  $^{12}\text{C}$  seems to conform to a superdeformed configuration in the secondary minimum.

The nucleus  $^{20}\text{C}$  which is highly oblate deformed ( $\beta_2 = -0.44$ ) with the force TM1 is also shown in Fig. 10. This value of the oblate deformation is close to the 2:3 ratio of the axes, whereby the axis of symmetry is accordingly shorter by this ratio.

In Fig. 11 we compare single-particle levels for  $^{10}\text{C}$  for the lowest energy state with those of the second minimum in energy for NL-SV1. As the second minimum state is very close

in energy (only  $\sim 0.5$  MeV above the lowest energy), it is instructive to see the difference in the single-particle structure of a shape-coexisting highly prolate and an oblate shape. For the highly prolate shape ( $\beta_2 \sim 0.59$ ), both the  $\Omega$  components of  $1p3/2$  level, i.e.  $[110]1/2^-$  and  $[101]3/2^-$  contribute to the prolate deformation, whereby the level  $[110]1/2^-$  plays a significant role. For the oblate shape, the orbital  $[101]3/2^-$  along with  $[101]1/2^-$  of  $1p1/2$  contribute to the deformation. Here the role of the level  $[110]1/2^-$  for the oblate shape becomes minimal. It is interesting to see a readjustment of various  $\Omega$  orbitals for two very different shapes but with almost the same total energy.

## V. SUMMARY AND CONCLUSIONS

We have investigated the ground-state properties of carbon isotopes in the framework of the relativistic mean-field theory using the self-couplings of  $\sigma$  and  $\omega$  mesons. Calculations performed in the axially deformed configuration show that many carbon isotopes except those with magic neutron numbers are significantly deformed. The force NL-SH with the scalar self-coupling is shown to give a highly deformed prolate shape for  $^{10}\text{C}$  in the lowest energy state. However, the forces NL-SV1 and TM1 with the scalar and vector self-couplings predict an oblate shape for this nucleus. An oblate shape for  $^{10}\text{C}$  is also shown to occur with NL-SH, however, in the secondary minimum. For  $^{12}\text{C}$ , the quadrupole deformation obtained with the various RMF forces is in good agreement with the values obtained from various experiments.

For all other isotopes above  $A=16$ , predictions on the deformation of nuclei are similar in the scalar self-coupling and scalar-vector self-coupling models. Both the models predict an oblate shape for the heavier carbon nuclei. The isotopes  $^{18}\text{C}$ ,  $^{20}\text{C}$  and  $^{22}\text{C}$  are predicted to be well deformed. The relative magnitude of the quadrupole deformations and quadrupole moments is largest for TM1 and it is seen that deformations produced by NL-SH are slightly smaller than those of NL-SV1. It is observed that NL-SH exhibits the phenomenon of shape coexistence for several carbon isotopes whereas such a feature is presented by TM1 and NL-

SV1 only for  $^{10}\text{C}$  where this nucleus is predicted to possess a very large prolate deformation in the secondary minimum lying only 0.5 MeV above the lowest energy state with NL-SV1 and 0.9 MeV above the lowest energy state with TM1.

The relative quadrupole deformations of the neutron and proton mean fields show that for lighter carbon isotopes, the neutron and proton fields have almost comparable deformations in all the models. However, isotopes above  $A=16$  show significant differences in the deformations of the neutron and proton mean fields. The quadrupole deformation for neutrons are found to be larger than the corresponding proton deformation for the heavier carbon isotopes. The magnitude of the difference in the neutron and proton deformations is higher with the forces with the scalar-vector self-coupling than with the scalar self-coupling alone.

The *rms* matter and neutron radii obtained with the scalar and scalar-vector self-coupling model in the RMF theory agree well with the experimental values on the matter and neutron radii deduced from the total reaction cross-sections. The neutron radii for the carbon isotopes show a gradual increase with an increase in the neutron number. Such a behaviour is predicted by all the forces we have employed. However, the increase in the neutron radius and consequently the radial extension of neutrons in space for very neutron-rich carbon nuclei is not so much as to characterize it as a neutron halo. This conclusion is in accord with the earlier results obtained on carbon nuclei using spherical relativistic Hartree-Bogoliubov calculations [34]. A similar statement can be made for carbon nuclei in the vicinity of the proton drip line that the proton halo for these nuclei is suppressed.

The single-particle structure and the occupancy of levels near Fermi surface show that in the midst of a large deformation for the nuclei  $^{18}\text{C}$ ,  $^{22}\text{C}$  and  $^{22}\text{C}$ , there is a pronounced gap in the shell structure. We have also looked into the levels which contribute significantly to a large value of deformation in these nuclei. It is shown that the magnitude of deformation in some carbon isotopes is akin to a superdeformation. The isotope  $^{20}\text{C}$  in its lowest energy state and  $^{10}\text{C}$  in the secondary minimum exemplify this behaviour. Such large deformations are produced predominantly in the scalar-vector self-coupling model. These predictions on

deformation properties change only a little from the force NL-SV1 to TM1.

## REFERENCES

- [1] E. Roeckel, Rep. Prog. Phys. **55** (1992) 1661.
- [2] A. Mueller and. B. Sherril, Ann. Rev. Nucl. Part. Sci. **43** (1993) 529.
- [3] I. Tanihata, Progr. Part. Nucl. Phys. **35** (1996) 435. (1995) 505.
- [4] J. Vervier, Prog. Part. Nucl. Phys. **37** (1996) 435.
- [5] Proc. 4th Int. Conf. on Radioactive Nuclear Beams, Omiya, Japan, Nucl. Phys. **A616** (1997).
- [6] I. Tanihata et al., Phys. Rev. Lett. **55** (1985) 2676.
- [7] M. Zhukov et al., Phys. Rep. **231** (1993) 151.
- [8] B.D. Serot and J.D. Walecka, Adv. Nucl. Phys. **16** (1986) 1.
- [9] P.G. Reinhard, Rep. Prog. Phys. **52** (1989) 439.
- [10] B.D. Serot, Rep. Prog. Phys. **55** (1992) 1855.
- [11] P. Ring, Prog. Part. Nucl. Phys. **37** (1996) 193.
- [12] B.D. Serot and J.D. Walecka, Mod. Phys. **E6** (1997) 515.
- [13] M.M. Sharma, M.A. Nagarajan, and P. Ring, Phys. Lett. **B312** (1993) 377.
- [14] M.M. Sharma, G.A. Lalazissis, and P. Ring, Phys. Lett. **B317** (1993) 9.
- [15] G.A. Lalazissis and M.M. Sharma, Nucl. Phys. **A586** (1995) 201.
- [16] G.A. Lalazissis, M.M. Sharma and P. Ring, Nucl. Phys. **A597** (1996) 35.
- [17] G.A. Lalazissis, A.R. Farhan and M.M. Sharma, Nucl. Phys. **A628** (1998) 221.
- [18] M.M. Sharma, G.A. Lalazissis, J. König, and P. Ring, Phys. Rev. Lett. **74** (1995) 3744.
- [19] E. Liatard et al. Europhys. Lett. **13** (1990) 401.

[20] Z. Ren, Z.Y. Zhu, Y.H. Cai and G. Xu, Nucl. Phys. **A605** (1996) 75.

[21] J. Boguta and A.R. Bodmer, Nucl. Phys. **A292** (1977) 413.

[22] R.J. Furnstahl, B.D. Serot and H.B. Tang, Nucl. Phys. **A598** (1996) 539.

[23] A.R. Bodmer, Nucl. Phys. **A526** (1991) 703.

[24] Y.K. Gambhir, P. Ring, and A. Thimet, Ann. Phys. (N.Y.) **198** (1990) 132.

[25] P. Möller and J.R. Nix, Nucl. Phys. **A536** (1992) 20.

[26] Y. Sugahara and H. Toki, Nucl. Phys. **A579** (1994) 557.

[27] M.M. Sharma (1998, unpublished)

[28] G. Audi and A.H. Wapstra, Nucl. Phys. **A565** (1993) 1.

[29] J. Specht, G.W. Schweimer, H. Rebel, G. Schatz, R. Lohken and G. Hauser, Nucl. Phys. **A171** (1971) 65.

[30] M. Yasue, T. Tanabe, F. Soga, T. Kodama, F. Shimokoshi, J. Kasagi, Y. Toba, Y. Kadota, T. Ohsawa and K. Furuno, Nucl. Phys. **A394** (1983) 29.

[31] P.J. Simmonds, K.I. Pearce, P.R. Hayes, N.M. Clarke, R.J. Griffiths, M.C. Mannion and C.A. Ogilvie, Nucl. Phys. **A482** (1988) 653.

[32] Y. Horikawa, Y. Torizuka, A. Nakada, S. Mitsunoba, Y. Kojima and M. Kimura, Phys. Lett. **36B** (1971) 9.

[33] H. de Vries, C.W. De Jager and C. de Vries, At. Data Nucl. Data Tables **36** (1987) 495.

[34] W. Pöschl, D. Vretenar, G.A. Lalazissis and P. Ring, Phys. Rev. Lett. **79** (1997) 3841.

[35] S.G. Nilsson and I. Ragnarsson, *Shape and Shells in Nuclear Structure*, (Cambridge University Press, 1995) p. 116.

## FIGURES

FIG. 1. The quadrupole deformation  $\beta_2$  (upper) and the corresponding quadrupole moment  $Q_2$  (lower) of the lowest energy ground-state in the RMF theory with (a) NL-SH (b) TM1 and (c) NL-SV1. The  $\beta_2$  and  $Q_2$  (mb) values of the shape-coexistent secondary minimum are shown by a circle enclosed by a square. The  $\beta_2$  values for  $^{12}\text{C}$  from Ref. [29] (diamond), Ref. [30] (triangle up) and from Ref. [31] (open circle) are also shown for comparison.

FIG. 2. The difference  $\beta_n - \beta_p$  in the quadrupole deformations of the neutron and proton mean-fields. Points with a secondary minimum are shown by a square.

FIG. 3. The *rms* neutron, matter and charge radii of C isotopes in the RMF theory obtained with the force (a) NL-SH with the scalar self-coupling. The neutron radius from RHB calculations of Ref. [34] is also shown. (b) Radii with TM1 and (c) Radii with NL-SV1 with the scalar and vector self-coupling.

FIG. 4. The L=0 component of the neutron vector (baryonic) density  $\rho_v$  (upper) and scalar density  $\rho_s$  (lower) with (a) NL-SH (b) TM1 (c) NL-SV1.

FIG. 5. The L=2 component of the neutron vector density  $\rho_v$  for a few deformed nuclei near neutron drip line with (a) NL-SH (b) TM1 and (c) NL-SV1.

FIG. 6. The L=0 component of the proton vector density  $\rho_v$  compared for proton-rich nuclei with (a) NL-SH (b) TM1 and (c) NL-SV1.

FIG. 7. The neutron single-particle levels with the force NL-SH. The lower panel shows the deeper lying  $\Omega$  orbitals, whereas the upper panel shows levels in the vicinity of the Fermi surface.

FIG. 8. The neutron single-particle levels with the force NL-SV1. The details are the same as for Fig. 7.

FIG. 9. The occupation probabilities for the highest five levels in the vicinity of the Fermi surface, for (a) NL-SH and (b) NL-SV1.

FIG. 10. The shapes of a few strongly deformed carbon isotopes. The upper panel shows the shape for the lowest energy state of  $^{10}\text{C}$  and  $^{20}\text{C}$ . In the lower panel the prolate deformation for the secondary minimum for  $^{10}\text{C}$  is shown. The vertical axis represents the axis of symmetry.

FIG. 11. The single-particle structure of the lowest energy state (oblate) and the highly deformed secondary minimum (prolate) for  $^{10}\text{C}$  using the force NL-SV1. The particle occupation numbers are given in the parentheses.

## TABLES

TABLE I. The Lagrangian parameters of the forces NL-SH, TM1 and NL-SV1 used in the RMF calculations.

|            | NL-SH     | TM1     | NL-SV1    |
|------------|-----------|---------|-----------|
| M          | 939.0     | 938.0   | 939.0     |
| $m_\sigma$ | 526.05921 | 511.198 | 510.03488 |
| $m_\omega$ | 783.0     | 783.0   | 783.      |
| $m_\rho$   | 763.0     | 770.0   | 763.      |
| $g_\sigma$ | 10.44355  | 10.0289 | 10.12479  |
| $g_\omega$ | 12.9451   | 12.6139 | 12.72661  |
| $g_\rho$   | 4.38281   | 4.6322  | 4.49197   |
| $g_2$      | -6.90992  | -7.2325 | -9.24058  |
| $g_3$      | -15.83373 | 0.6183  | -15.388   |
| $g_4$      | 0.0       | 71.5075 | 41.01023  |

TABLE II. The binding energies (in MeV) of even-even C isotopes obtained for the lowest energy state with the forces NL-SH, TM1 and NL-SV1. The empirical values (expt.) available are also shown for comparison. The numbers in the parentheses indicate the existence of a secondary minimum in the vicinity of the lowest-energy ground-state.

| A  | NL-SH           | TM1           | NL-SV1        | expt.  |
|----|-----------------|---------------|---------------|--------|
| 10 | -60.4 (-59.8)   | -60.2 (-59.3) | -57.9 (-57.4) | -60.3  |
| 12 | -89.6 (-89.5)   | -90.1         | -87.6         | -92.2  |
| 14 | -106.6          | -106.9        | -104.4        | -105.3 |
| 16 | -112.3          | -112.4        | -109.6        | -110.8 |
| 18 | -117.0 (-116.9) | -118.6        | -114.4        | -115.7 |
| 20 | -121.8          | -123.4        | -118.5        | -119.2 |
| 22 | -122.7 (-122.4) | -123.9        | -118.6        | -120.3 |
| 24 | -122.3          | -122.7        | -116.6        |        |

TABLE III. The quadrupole deformation  $\beta_2$  and the quadrupole moment  $Q_2$  (mb) obtained in the RMF theory for the C isotopes.

| A  | $\beta_2$      |                |                | $Q_2$          |               |              |
|----|----------------|----------------|----------------|----------------|---------------|--------------|
|    | NL-SH          | TM1            | NL-SV1         | NL-SH          | TM1           | NL-SV1       |
| 10 | 0.536 (-0.161) | -0.294 (0.643) | -0.213 (0.584) | 85.5 (-25.7)   | -46.9 (102.6) | -33.9 (93.1) |
| 12 | -0.23 (0.005)  | -0.388         | -0.328         | -50.6 (0.9)    | -83.9         | -70.9        |
| 14 | 0.000          | 0.011          | 0.005          | 0.14           | 0.3           | 0.14         |
| 16 | -0.005         | -0.006         | 0.004          | -1.6           | -2.2          | 1.2          |
| 18 | -0.316 (0.387) | -0.354         | -0.325         | -134.3 (164.3) | -150.4        | -137.9       |
| 20 | -0.405         | -0.444         | -0.418         | -205.3         | -224.7        | -211.6       |
| 22 | -0.308 (0.029) | -0.367         | -0.336         | -183.2 (17.1)  | -217.9        | -199.3       |
| 24 | -0.006         | -0.16          | -0.07          | -4.0           | -112.8        | -49.4        |

TABLE IV. The *rms* neutron radii  $r_n$  and matter radii  $r_m$  (in fm) as obtained in the RMF theory for various RMF forces. The experimental values [19] deduced from total reaction cross-sections are also shown for comparison

| A  | $r_n$ |      |        |                 | $r_m$ |      |        |                 |
|----|-------|------|--------|-----------------|-------|------|--------|-----------------|
|    | NL-SH | TM1  | NL-SV1 | expt.           | NL-SH | TM1  | NL-SV1 | expt.           |
| 10 | 2.49  | 2.49 | 2.48   |                 | 2.69  | 2.69 | 2.67   |                 |
| 12 | 2.50  | 2.57 | 2.56   | $2.49 \pm 0.16$ | 2.52  | 2.59 | 2.57   | $2.48 \pm 0.08$ |
| 14 | 2.57  | 2.59 | 2.60   | $2.70 \pm 0.10$ | 2.54  | 2.56 | 2.56   | $2.62 \pm 0.06$ |
| 16 | 3.01  | 3.03 | 3.04   | $2.89 \pm 0.09$ | 2.83  | 2.85 | 2.85   | $2.76 \pm 0.06$ |
| 18 | 3.18  | 3.22 | 3.24   | $3.06 \pm 0.29$ | 2.98  | 3.01 | 3.02   | $2.90 \pm 0.19$ |
| 20 | 3.32  | 3.37 | 3.35   |                 | 3.11  | 3.16 | 3.13   |                 |
| 22 | 3.47  | 3.52 | 3.54   |                 | 3.25  | 3.30 | 3.31   |                 |
| 24 | 3.59  | 3.63 | 3.66   |                 | 3.35  | 3.40 | 3.42   |                 |

TABLE V. The charge radius  $r_c$  obtained with various RMF forces. The experimental values for  $^{12}\text{C}$  and  $^{14}\text{C}$  from the electron scattering data [33] are also shown.

| A  | $r_c$ |      |        |                 |
|----|-------|------|--------|-----------------|
|    | NL-SH | TM1  | NL-SV1 | expt.           |
| 10 | 2.93  | 2.92 | 2.91   |                 |
| 12 | 2.66  | 2.73 | 2.71   | $2.47 \pm 0.02$ |
| 14 | 2.62  | 2.64 | 2.63   | $2.56 \pm 0.05$ |
| 16 | 2.62  | 2.64 | 2.63   |                 |
| 18 | 2.64  | 2.67 | 2.66   |                 |
| 20 | 2.66  | 2.7  | 2.68   |                 |
| 22 | 2.67  | 2.72 | 2.7    |                 |
| 24 | 2.66  | 2.72 | 2.69   |                 |

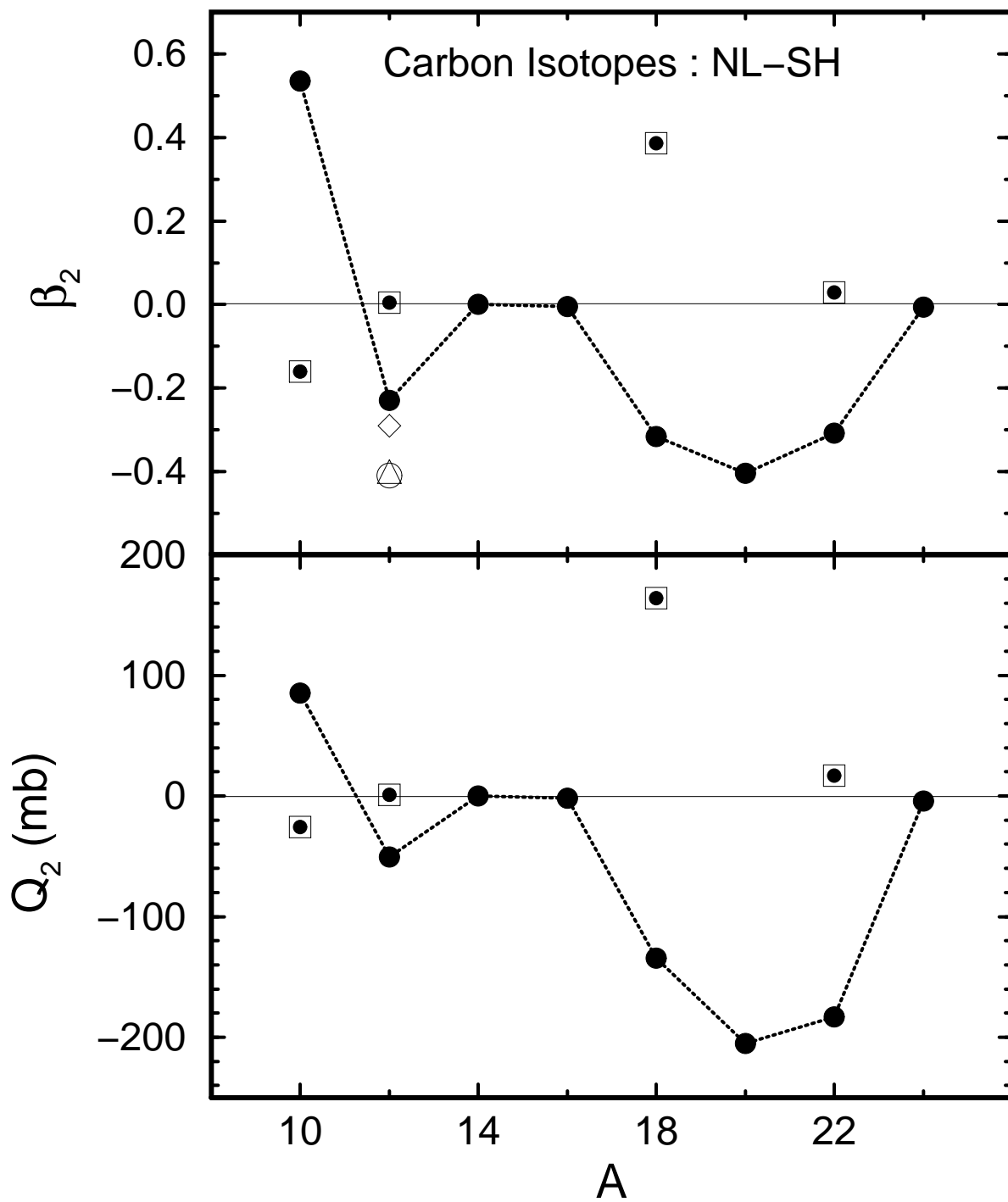


Fig. 1a

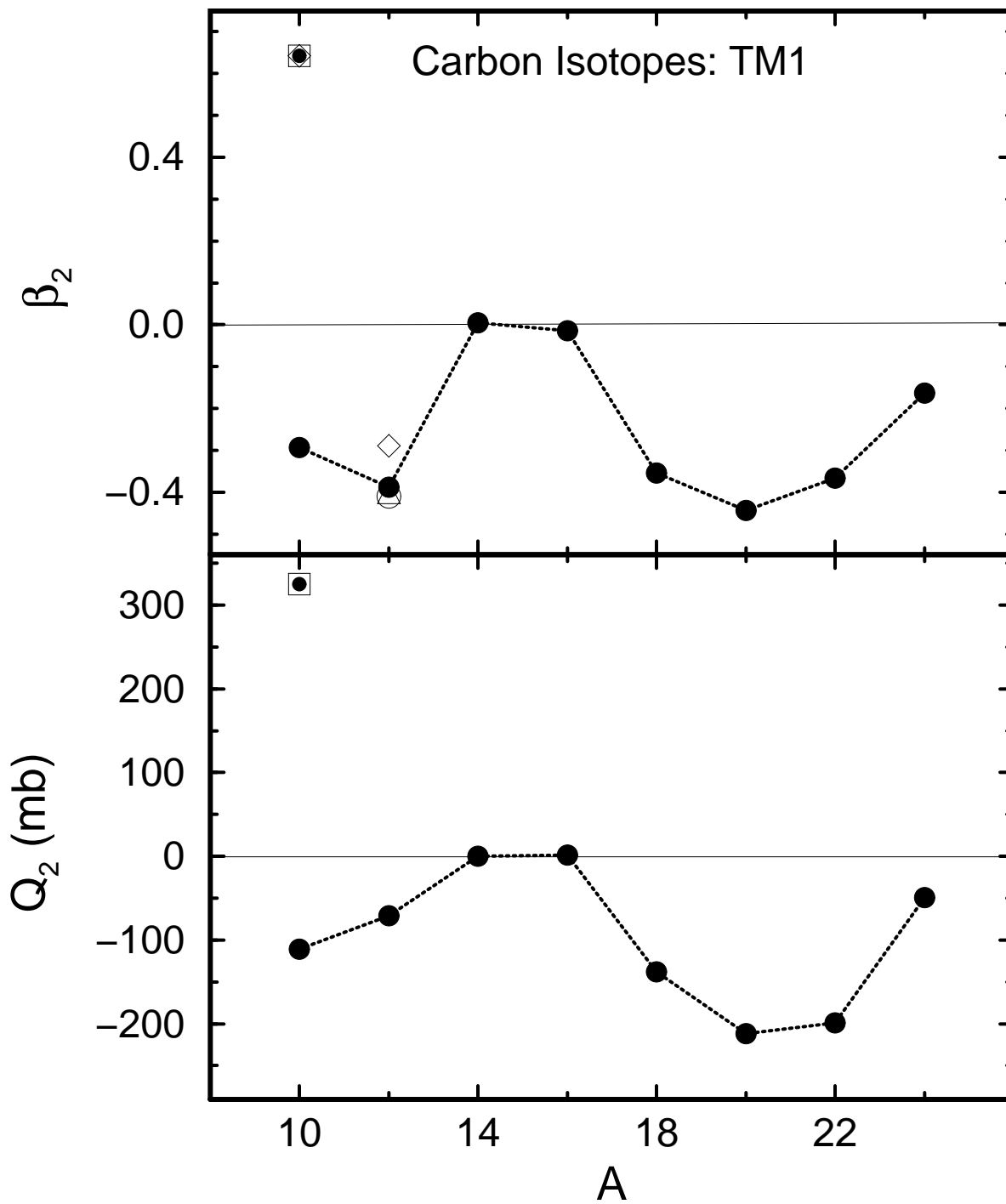


Fig. 1b

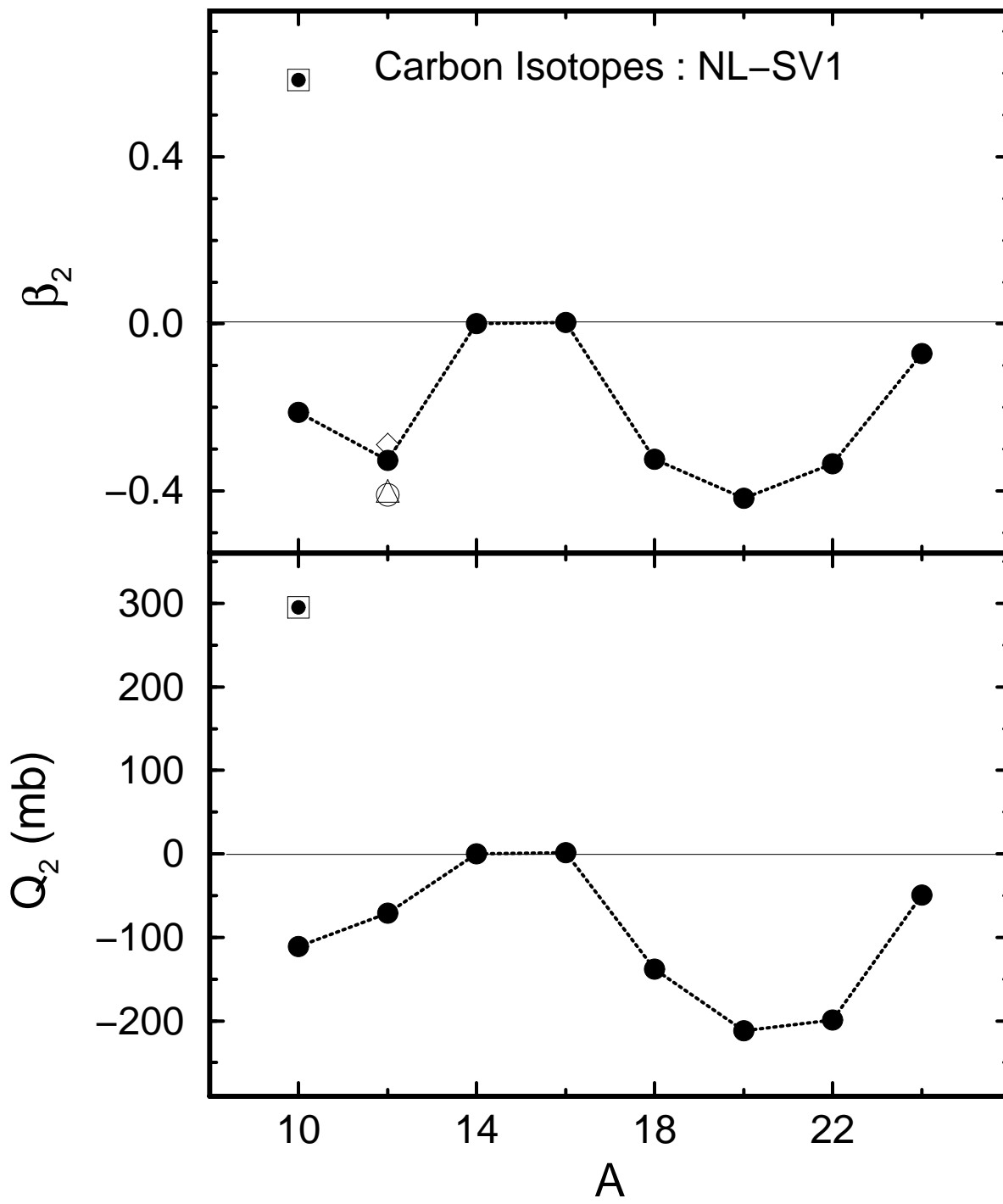


Fig. 1c

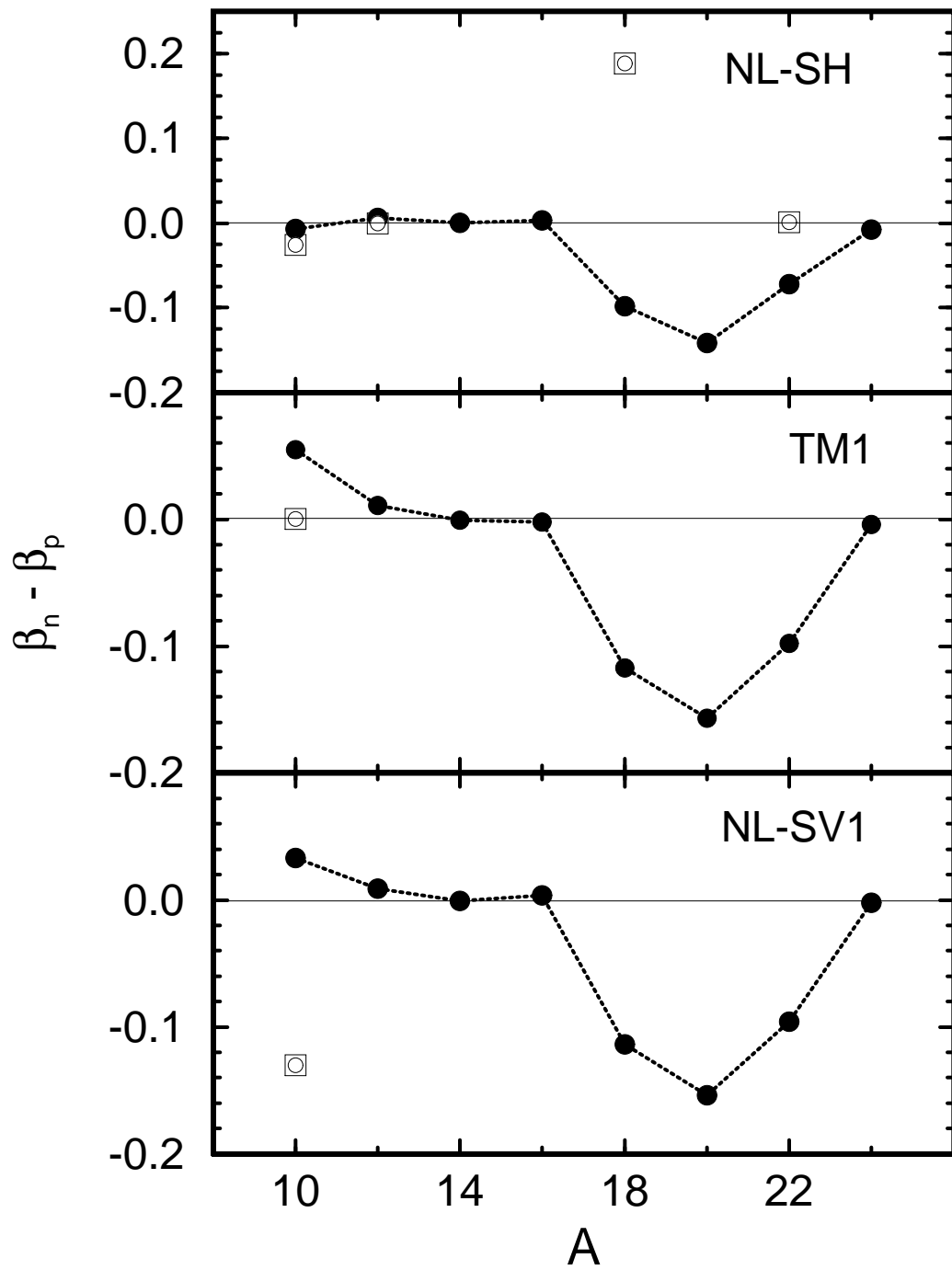
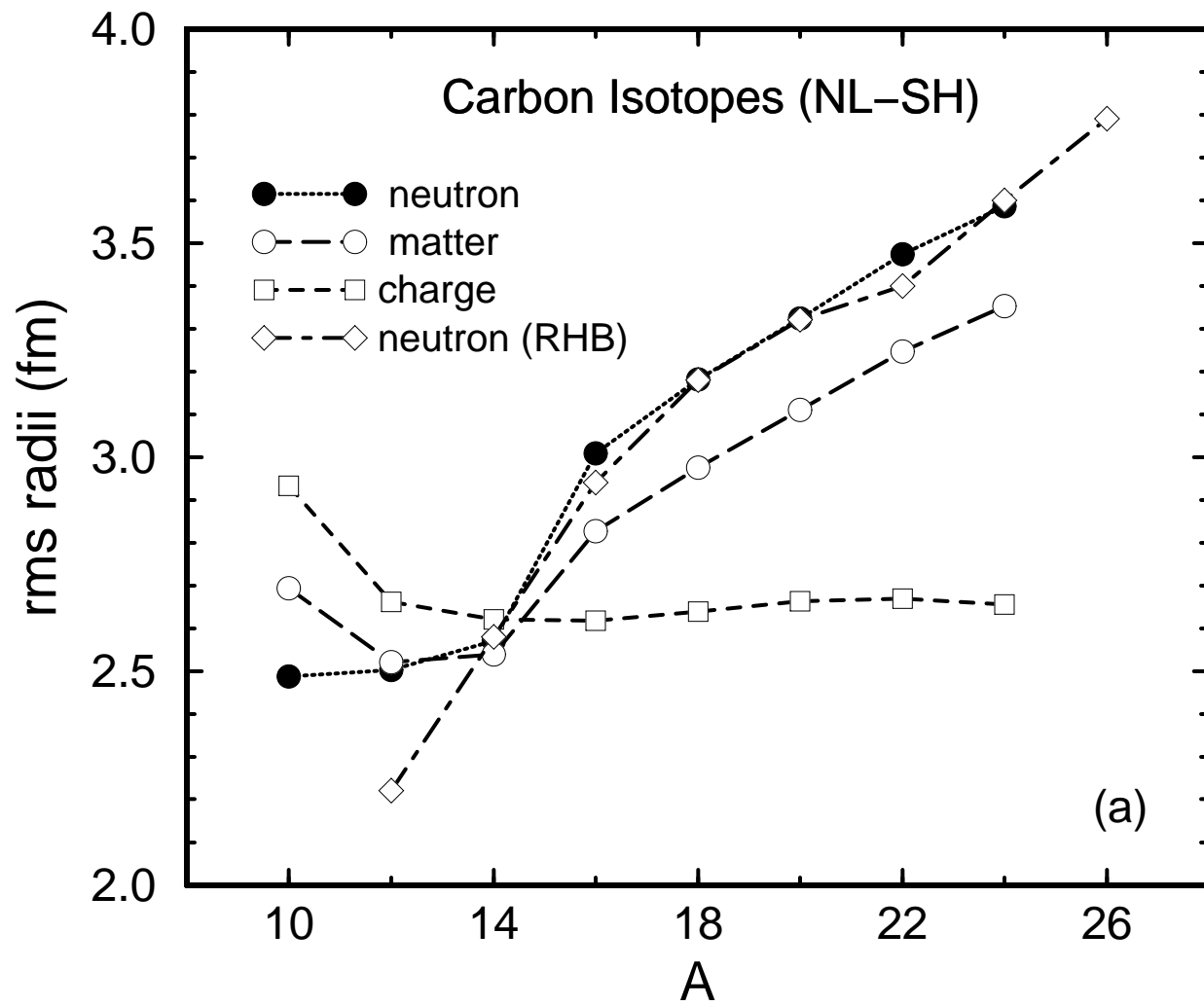


Fig. 2



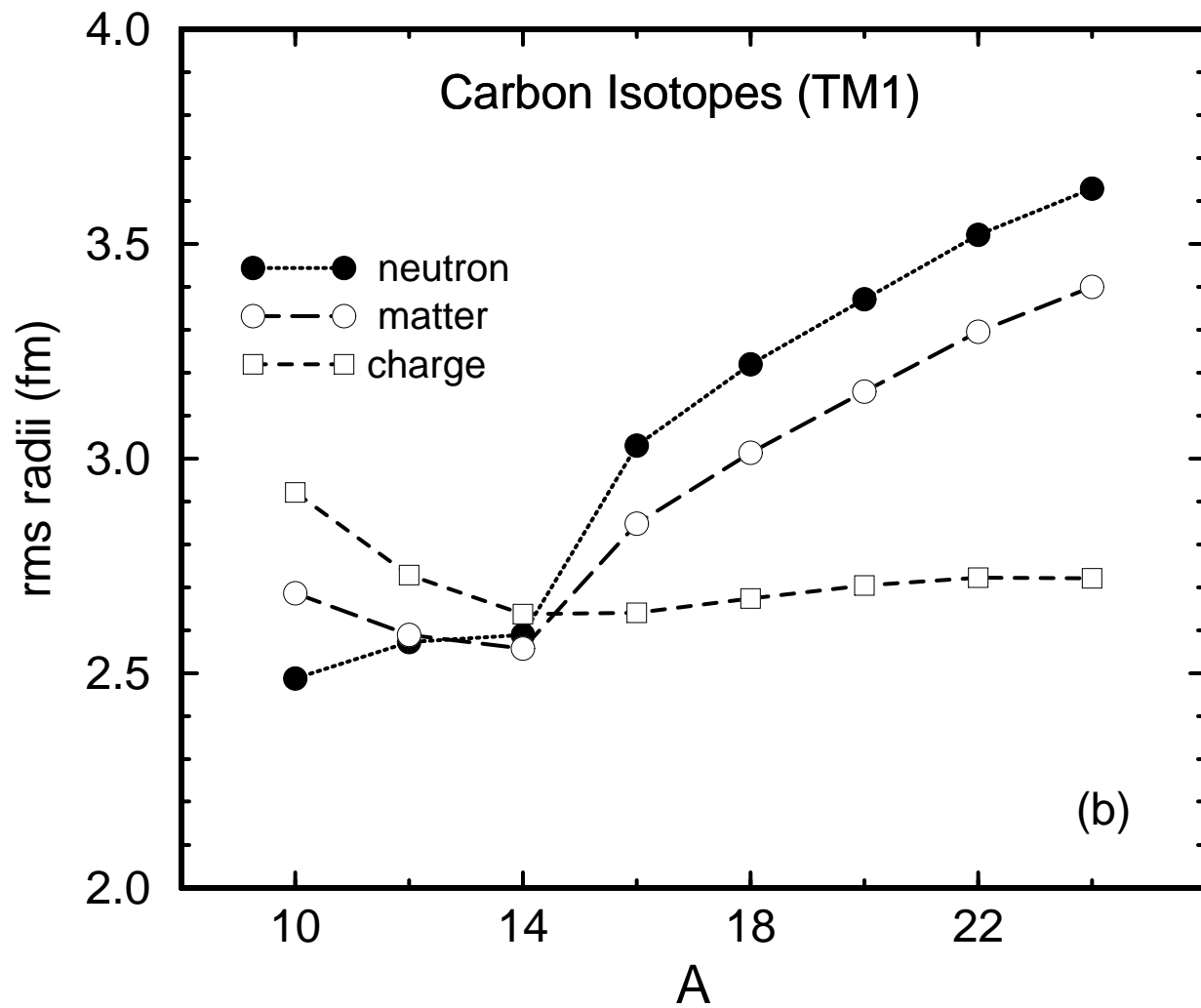


Fig. 3b

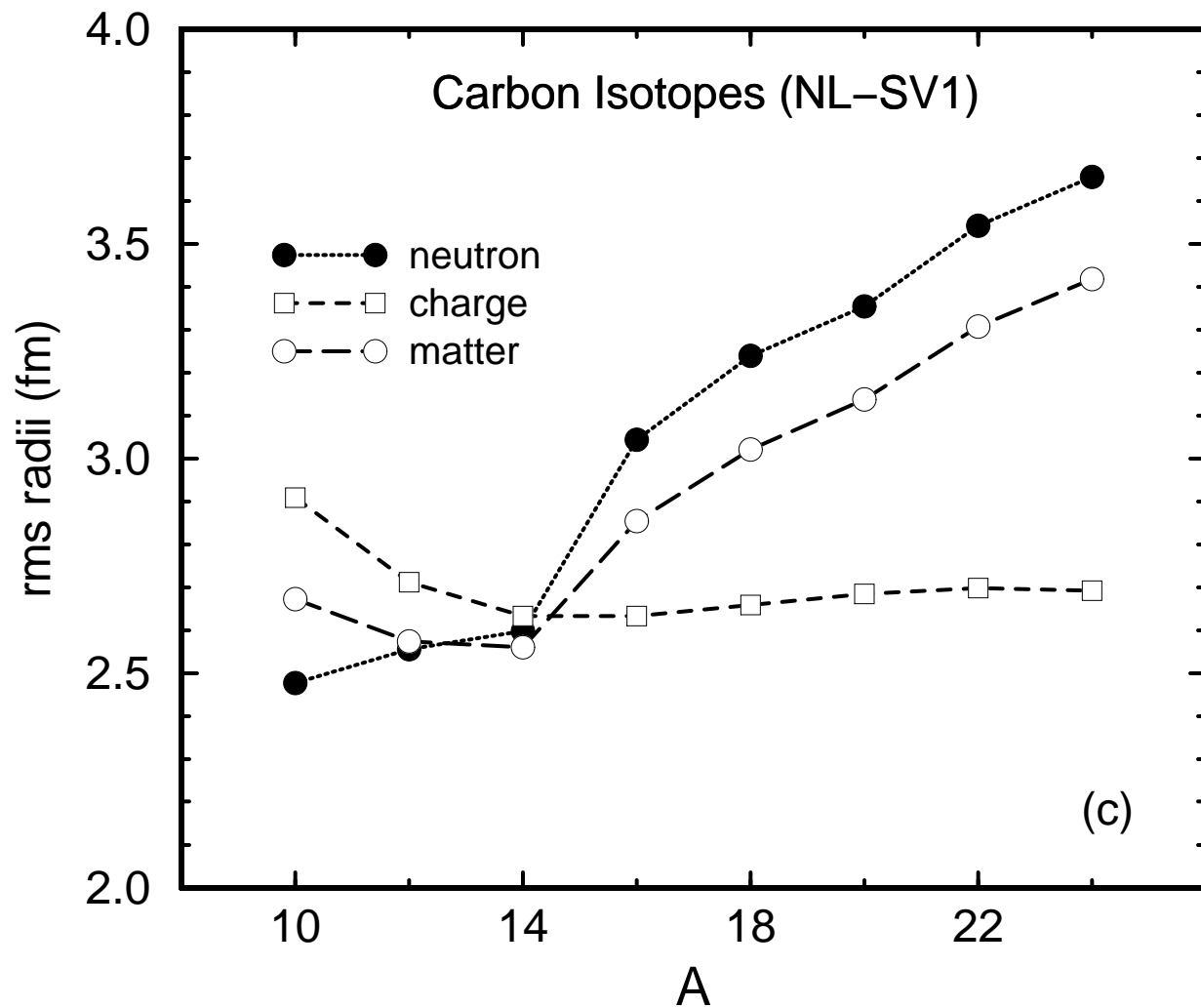


Fig. 3c

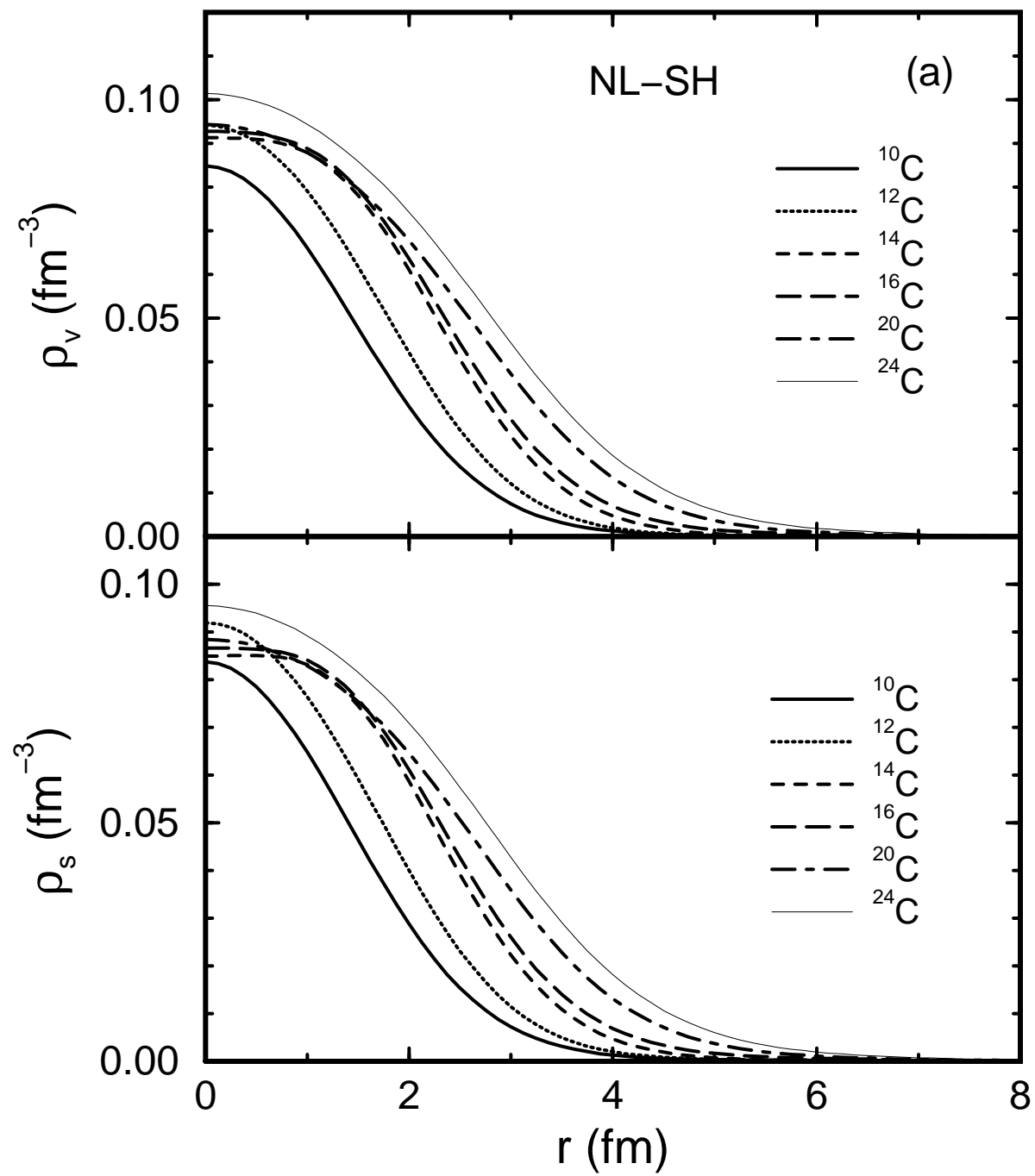


Fig. 4a

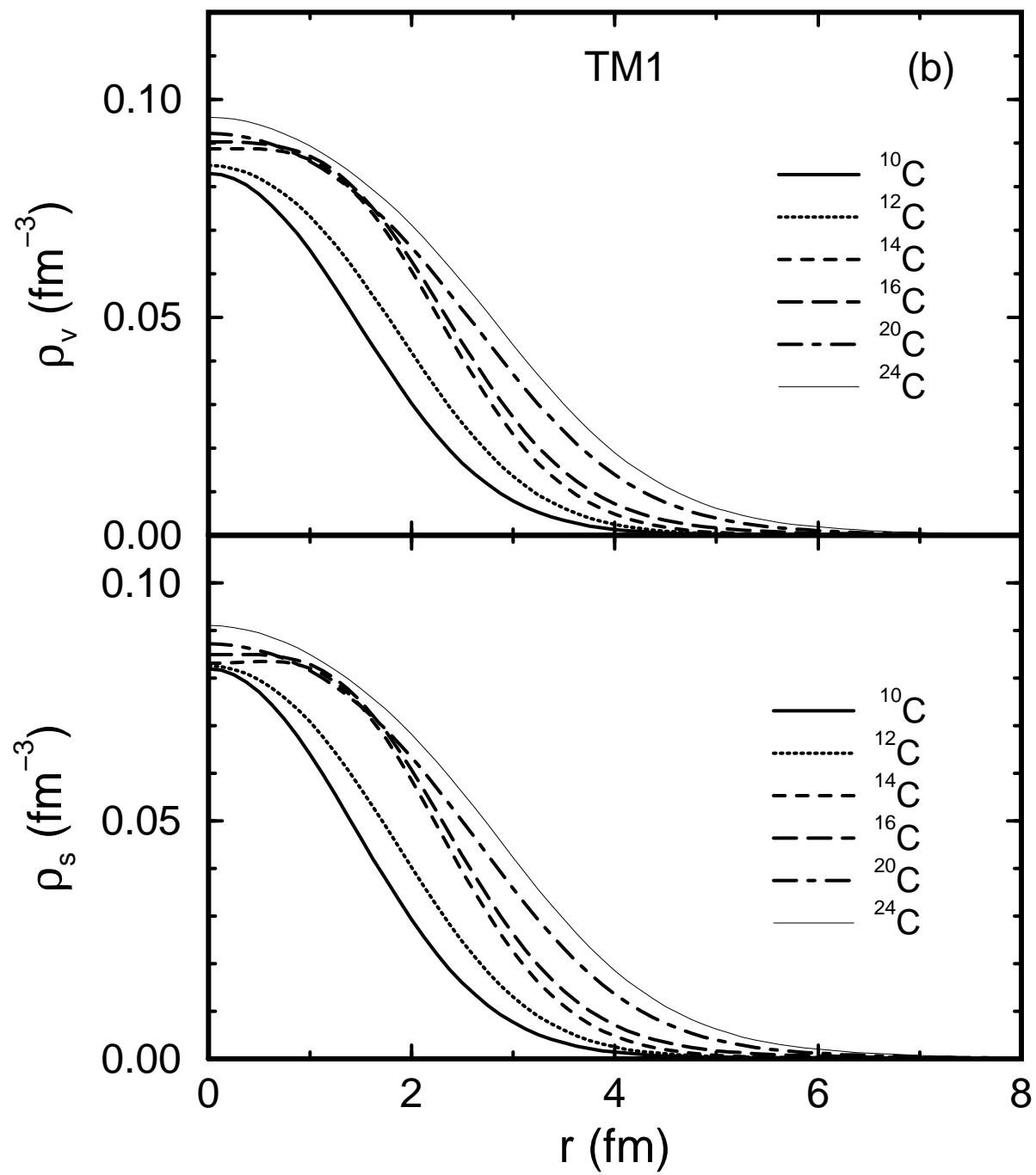


Fig. 4b

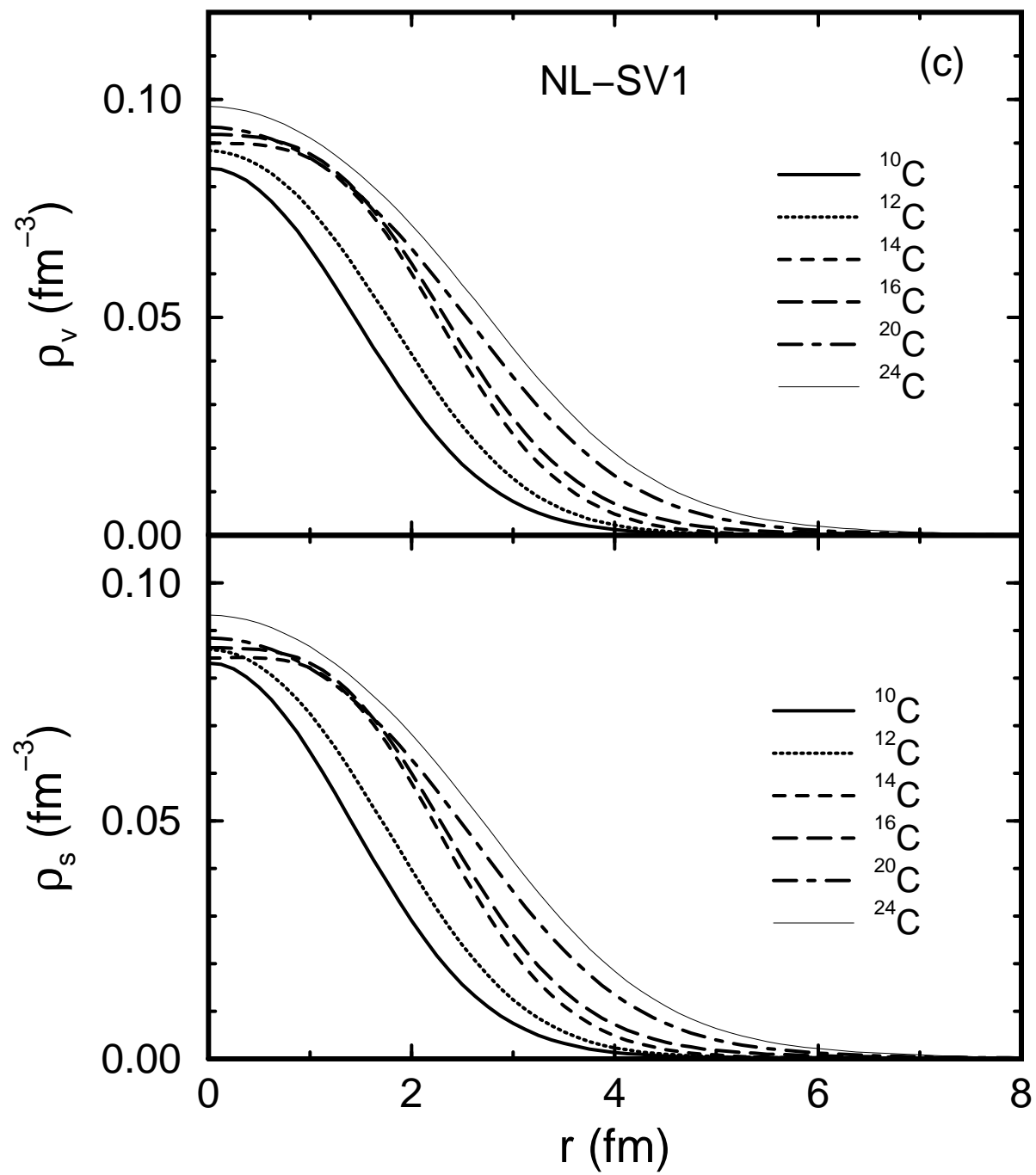


Fig. 4c

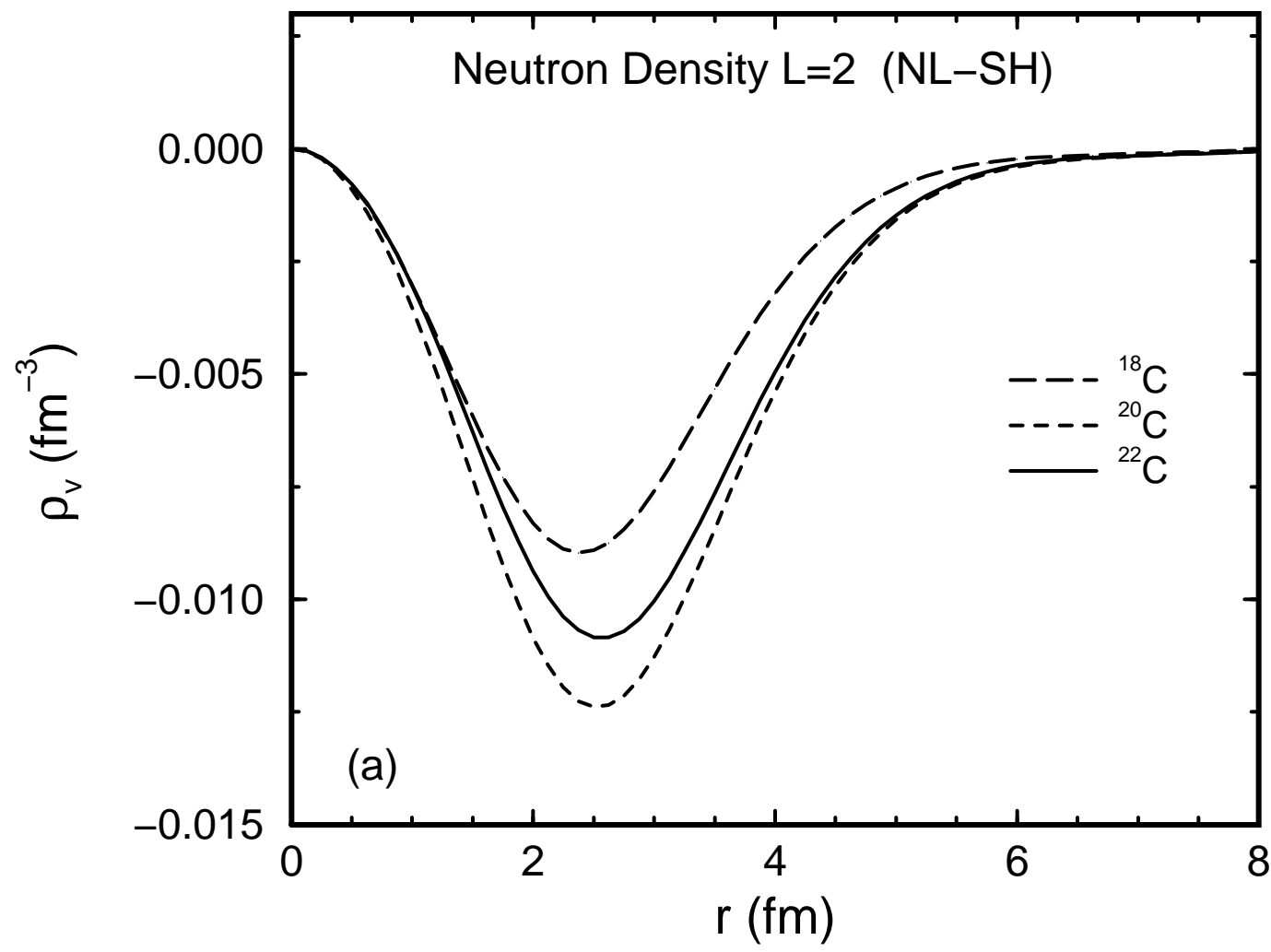


Fig. 5a

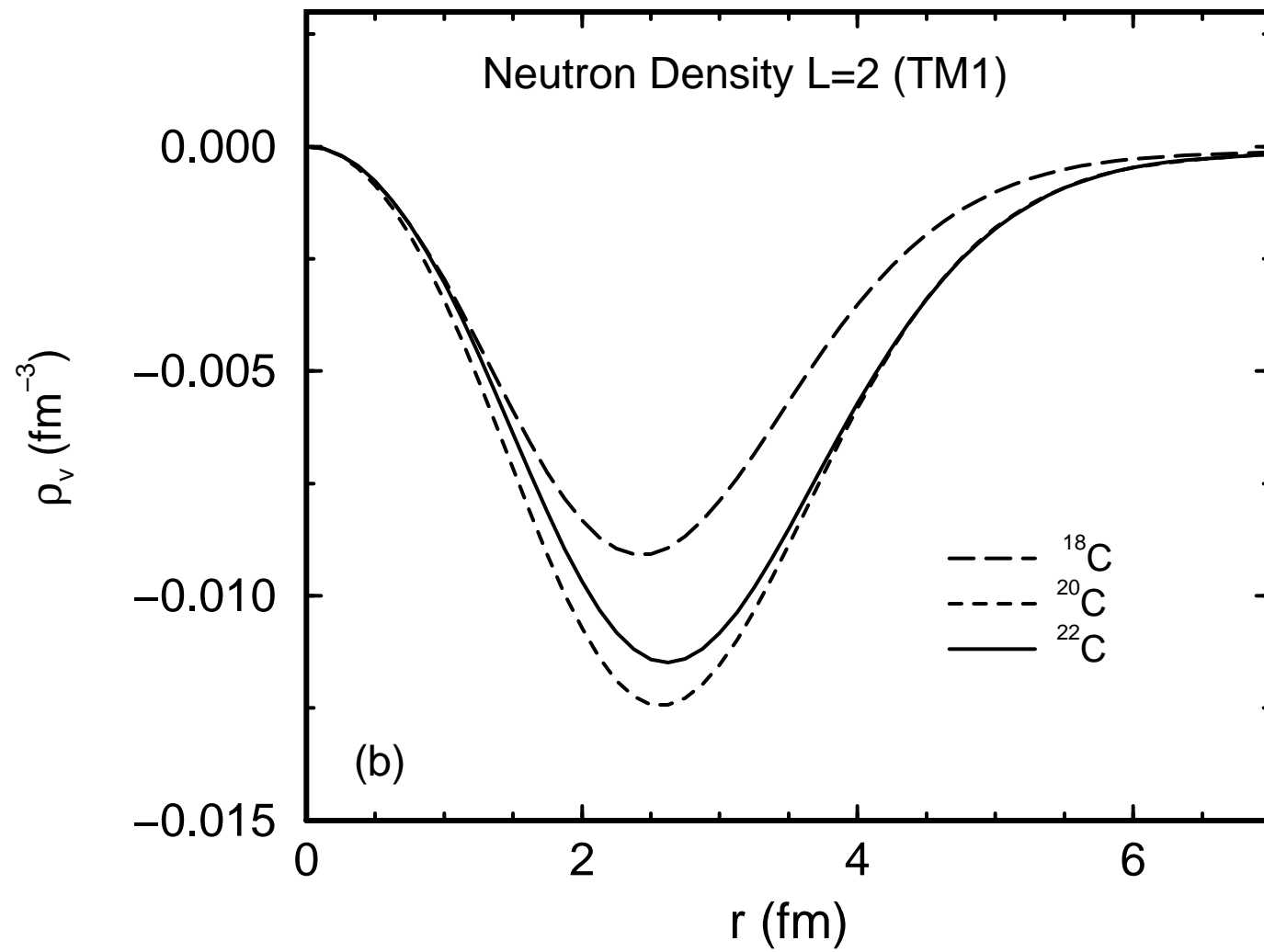


Fig. 5b

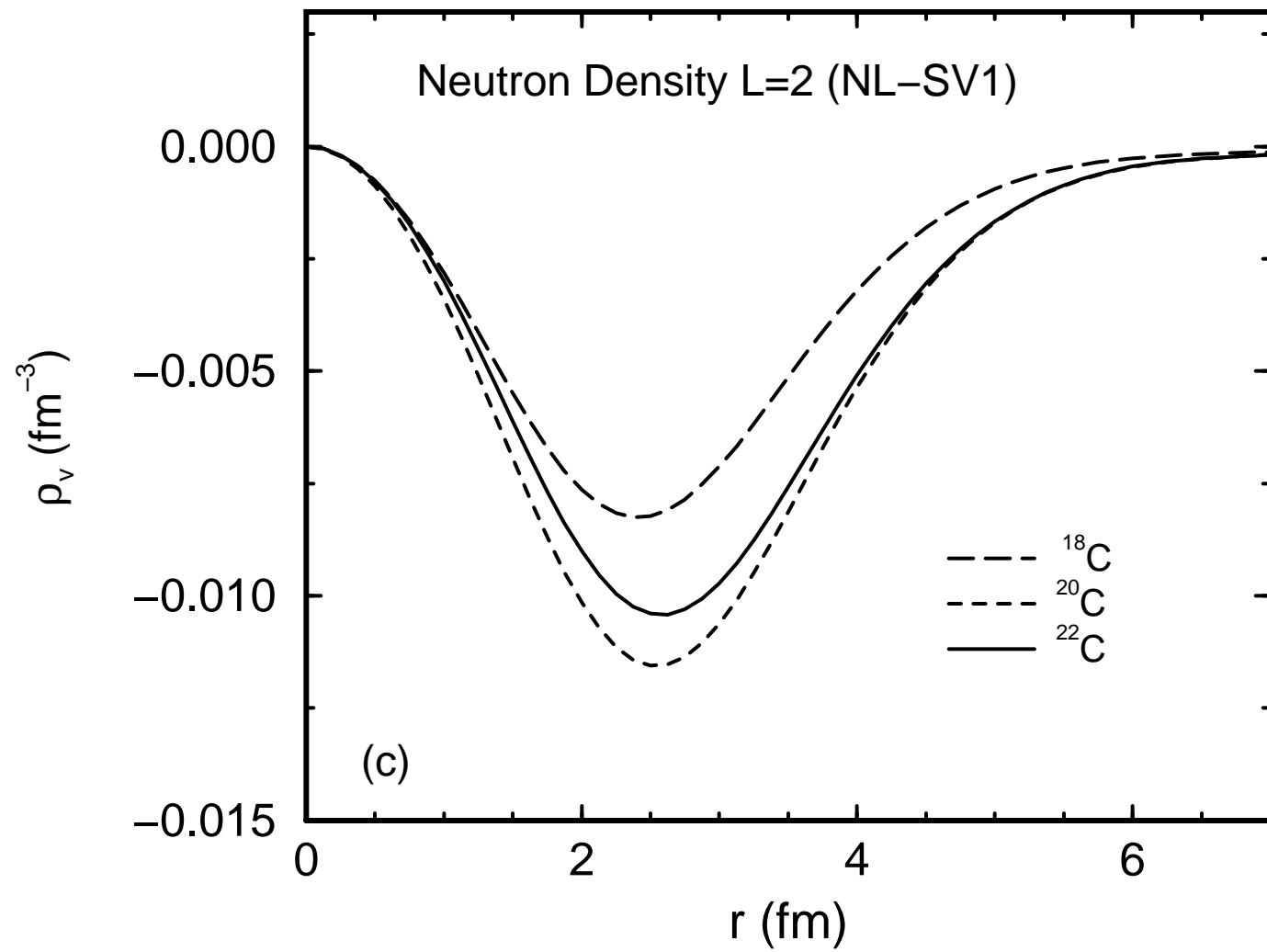
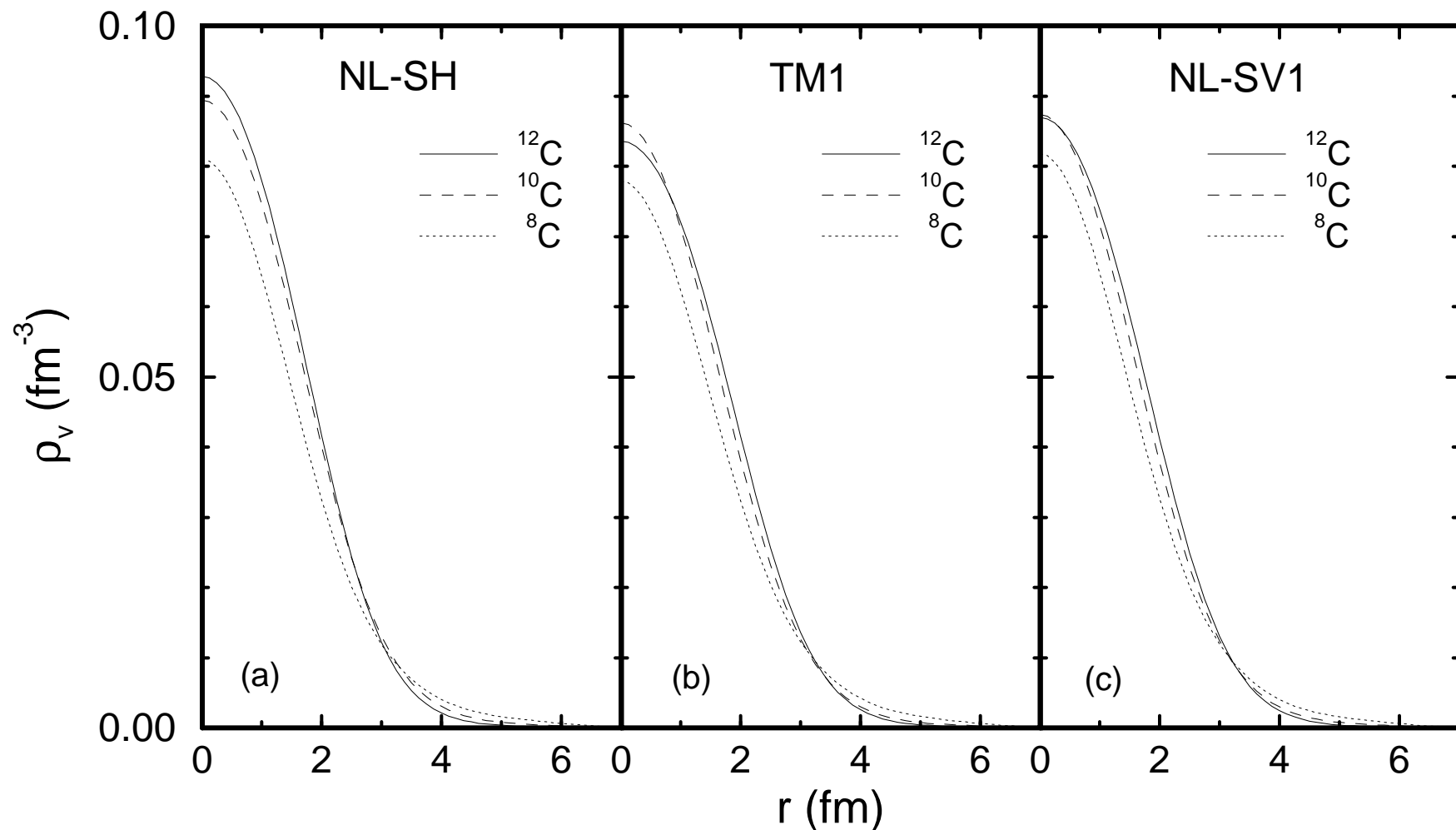


Fig. 5c

Fig. 6



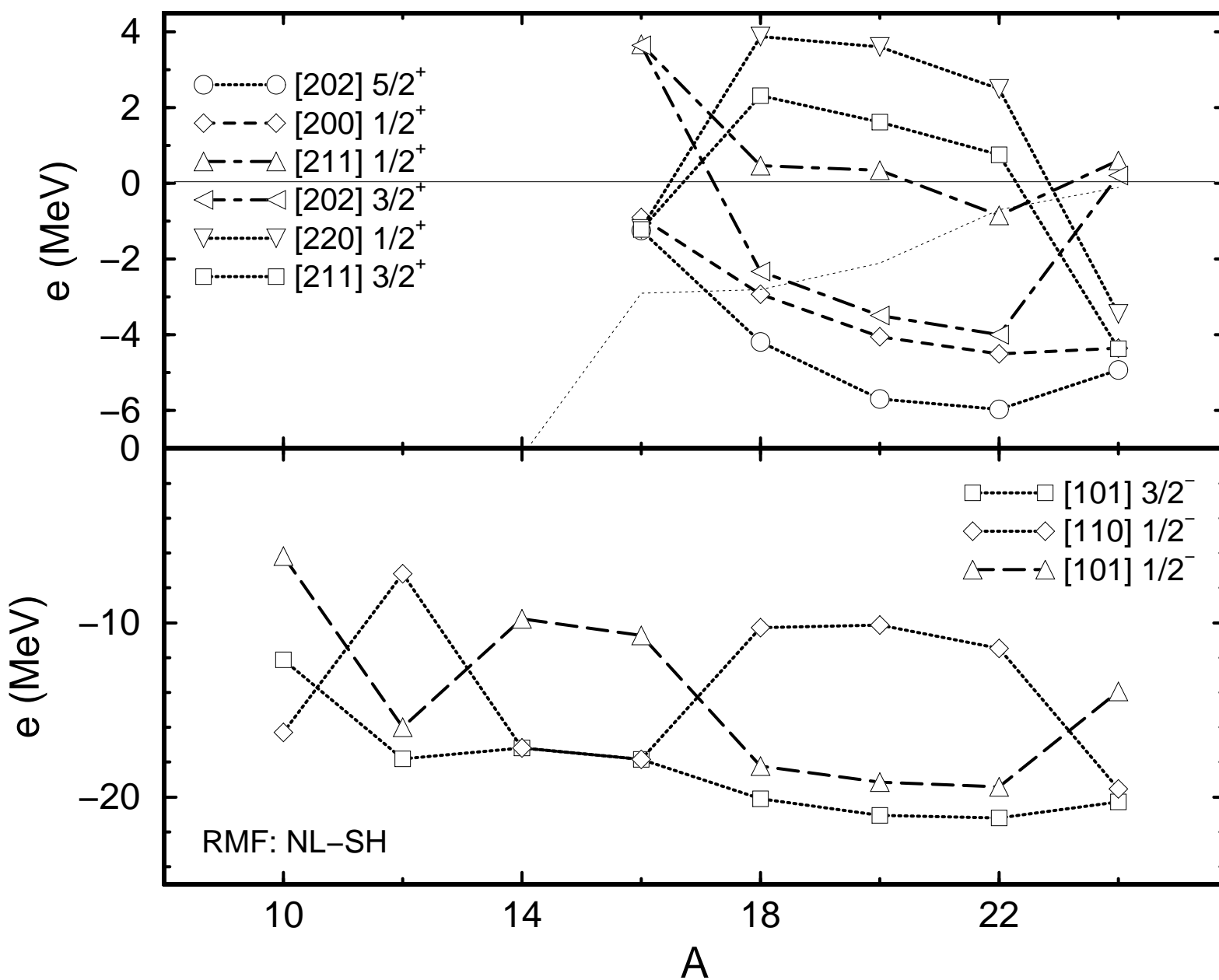


Fig . 7

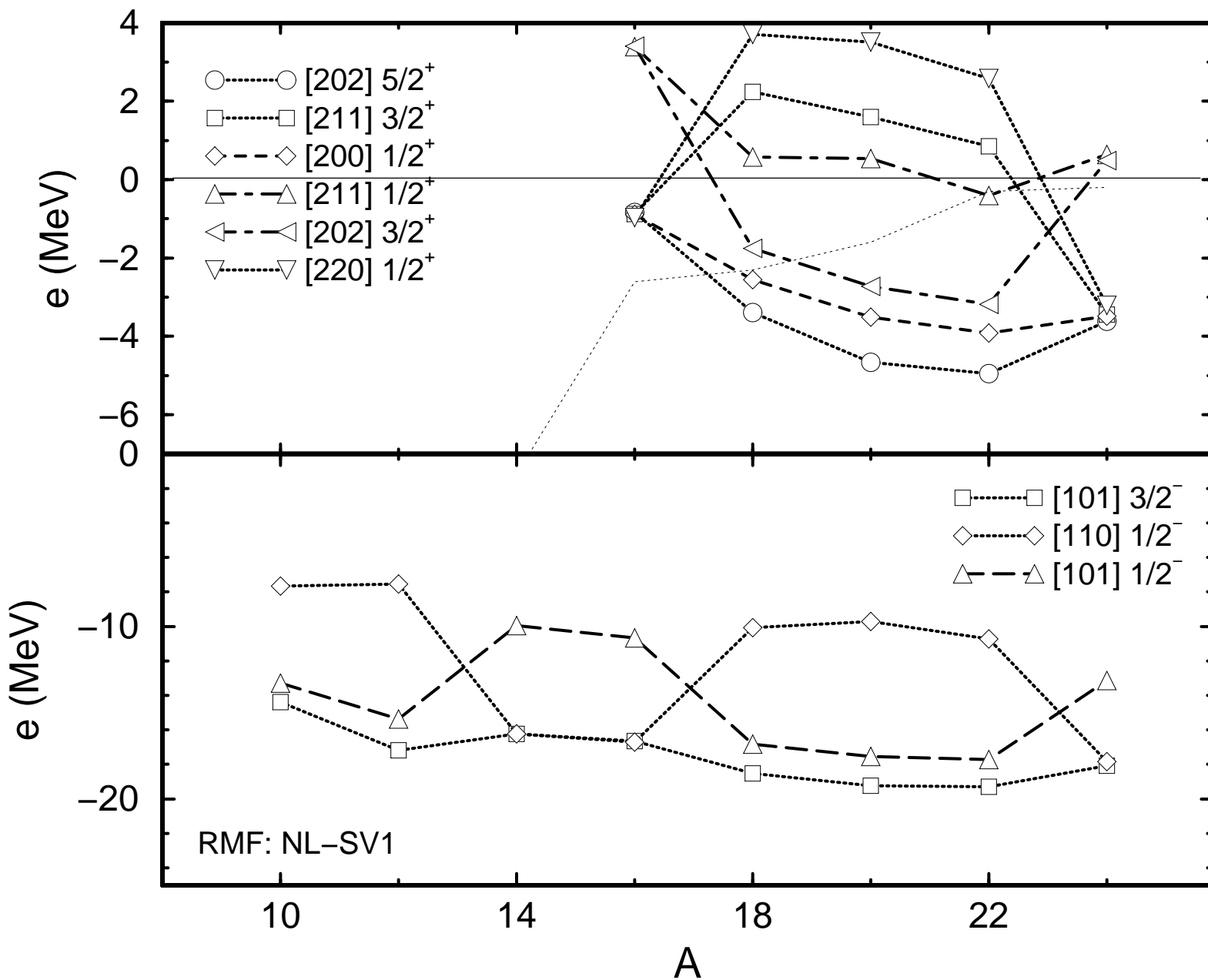


Fig. 8

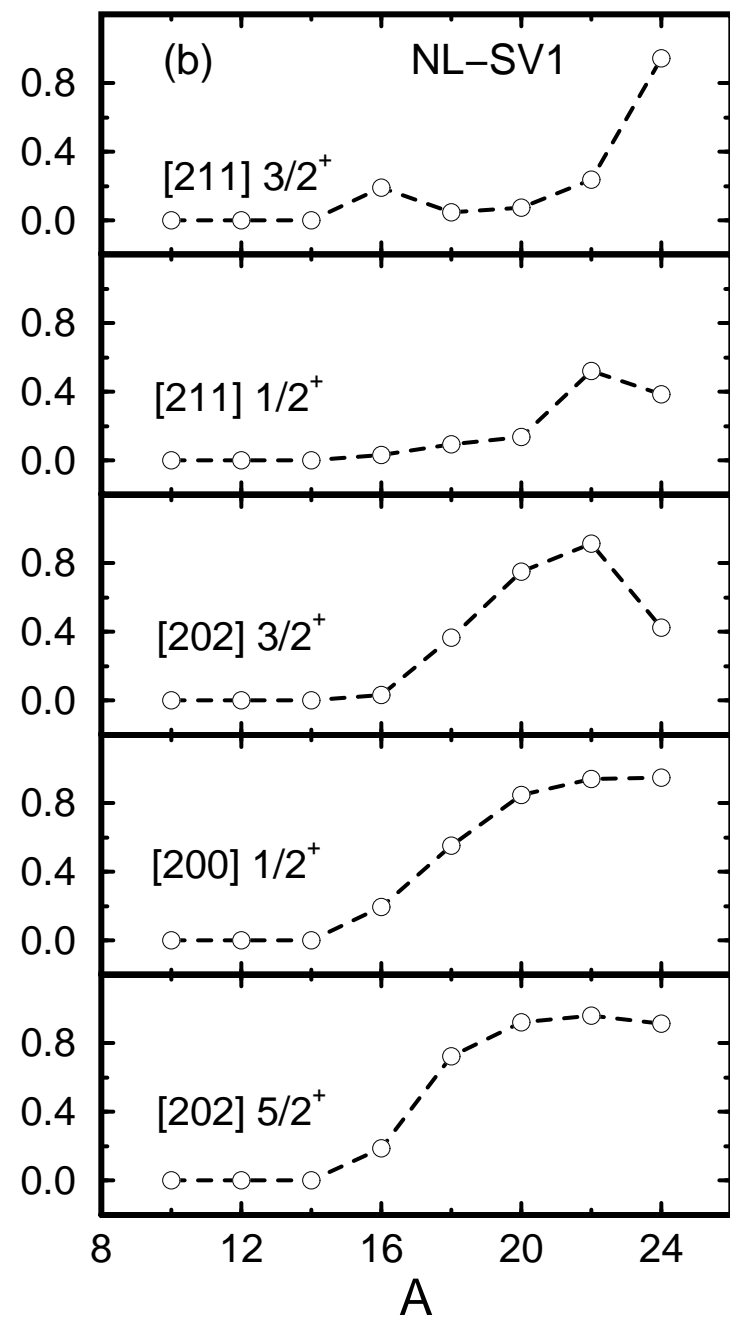
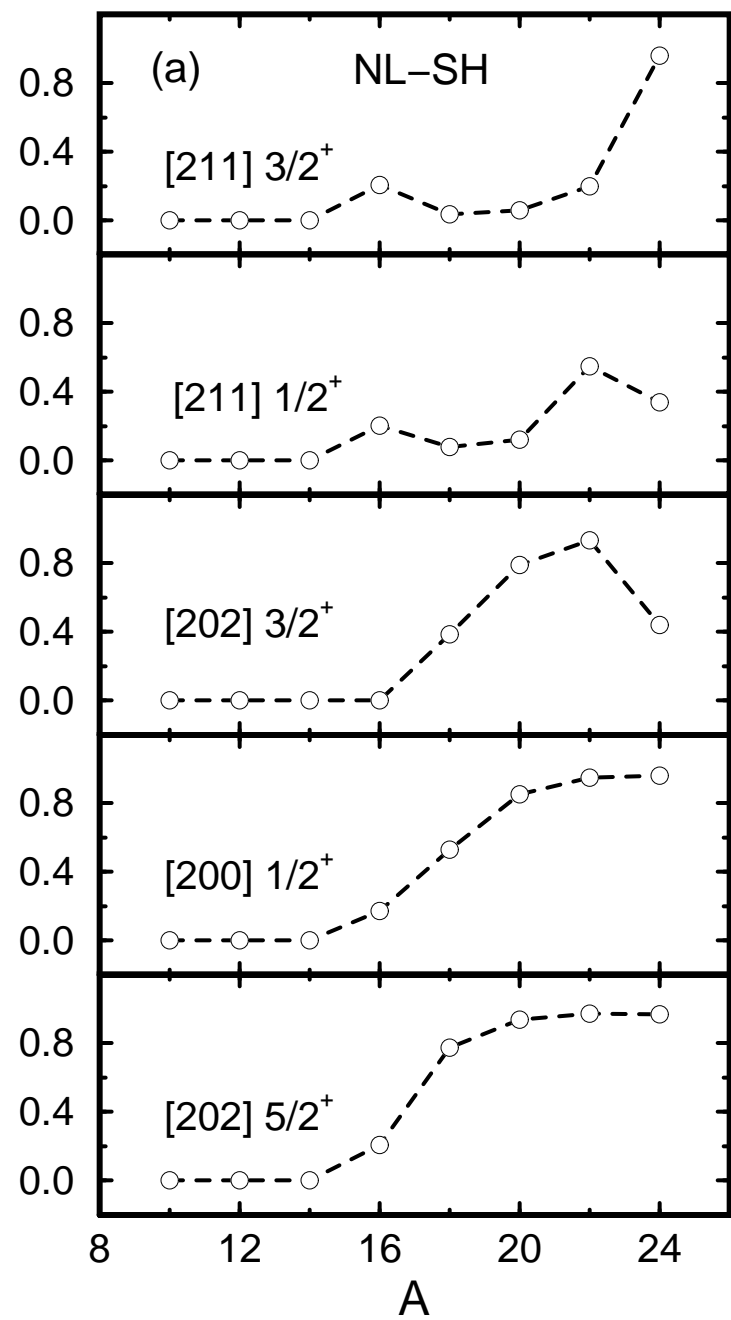


Fig . 9

$^{10}\text{C}$  (NL-SV1)

$^{10}\text{C}$  (TM1)

$^{20}\text{C}$  (TM1)

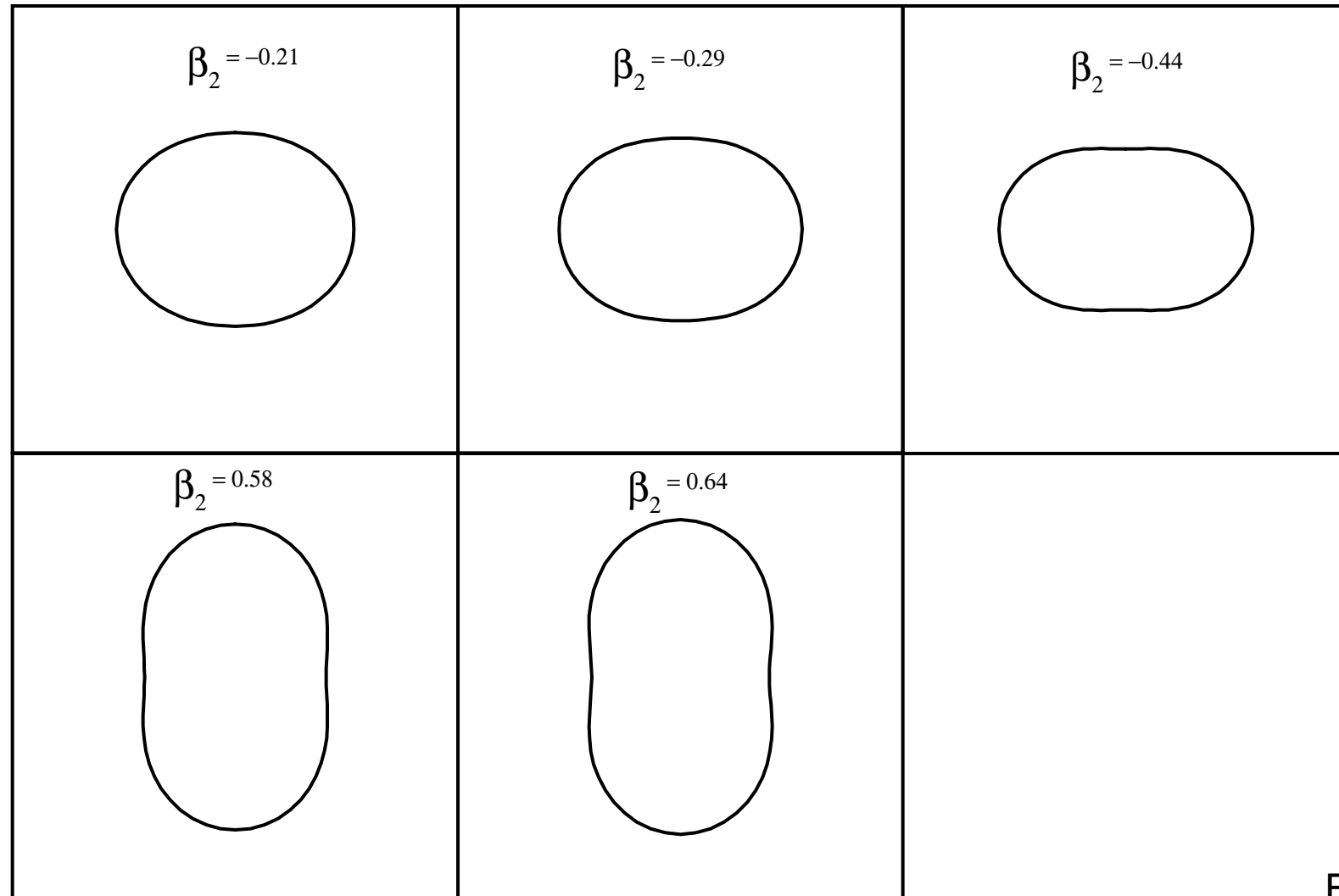


Fig. 10

Fig. 11

